iScience

CellPress
OPEN ACCESS

Article

Optic Atrophy 1 Controls Human Neuronal Development by Preventing Aberrant Nuclear DNA Methylation

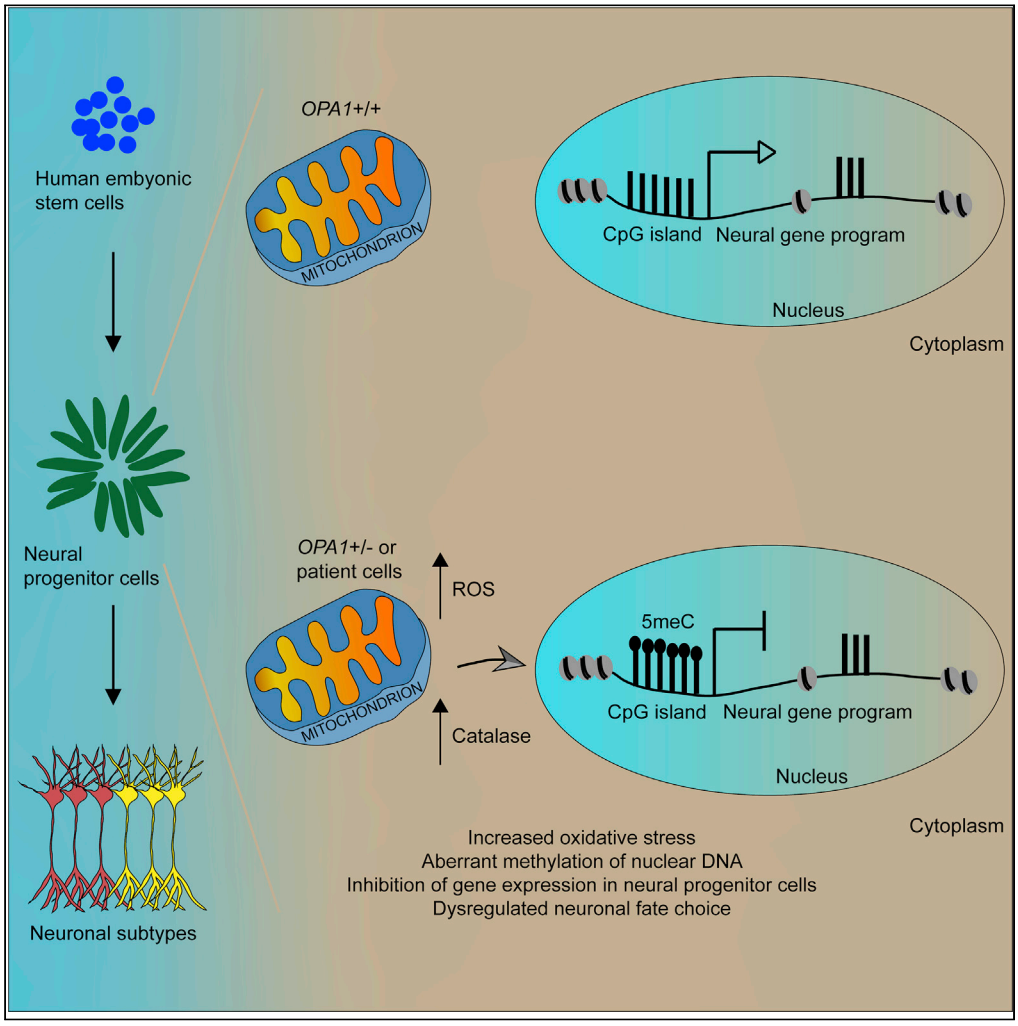

Safak Caglayan, Adnan Hashim, Artur Cieslar-Pobuda, ..., Antonella Boschi, Kjetil Taskén, Judith Staerk

judith.staerk@ncmm.uio.no

HIGHLIGHTS

OPA1 haploinsufficiency impairs formation of DLX1/2-positive GABAergic neurons

Reduced OPA1 levels significantly alter the transcriptional circuitry in neural cells

Expression of the pioneer factor *FOXG1* is decreased in *OPA1+/–* neural progenitor cells

Impaired *FOXG1* expression correlates with increased CpG methylation at its promoter

Caglayan et al., iScience *23*, 101154
June 26, 2020
https://doi.org/10.1016/j.isci.2020.101154

iScience

CellPress
OPEN ACCESS

Article

Optic Atrophy 1 Controls Human Neuronal Development by Preventing Aberrant Nuclear DNA Methylation

Safak Caglayan,[1] Adnan Hashim,[1] Artur Cieslar-Pobuda,[1] Vidar Jensen,[2] Sidney Behringer,[3] Burcu Talug,[1] Dinh Toi Chu,[1] Christian Pecquet,[4,5] Marie Rogne,[1] Andreas Brech,[6] Sverre Henning Brorson,[7] Erlend Arnulf Nagelhus,[2] Luciana Hannibal,[3] Antonella Boschi,[8] Kjetil Taskén,[1,9,10] and Judith Staerk[1,11,12,*]

SUMMARY

Optic atrophy 1 (OPA1), a GTPase at the inner mitochondrial membrane involved in regulating mitochondrial fusion, stability, and energy output, is known to be crucial for neural development: *Opa1* heterozygous mice show abnormal brain development, and inactivating mutations in OPA1 are linked to human neurological disorders. Here, we used genetically modified human embryonic and patient-derived induced pluripotent stem cells and reveal that *OPA1* haploinsufficiency leads to aberrant nuclear DNA methylation and significantly alters the transcriptional circuitry in neural progenitor cells (NPCs). For instance, expression of the forkhead box G1 transcription factor, which is needed for GABAergic neuronal development, is repressed in *OPA1+/−* NPCs. Supporting this finding, *OPA1+/−* NPCs cannot give rise to GABAergic interneurons, whereas formation of glutamatergic neurons is not affected. Taken together, our data reveal that OPA1 controls nuclear DNA methylation and expression of key transcription factors needed for proper neural cell specification.

INTRODUCTION

Mitochondria are double-membrane-bound subcellular organelles required for numerous cellular functions. In response to metabolic and physiological signals, mitochondria undergo fusion and fission, processes that are catalyzed by conserved GTP-hydrolyzing enzymes and their associated proteins (Chan, 2012). Fission of mitochondria is needed for their fragmentation. This is triggered by dynamin 1-like protein (DNM1L), a cytoplasmic protein that is recruited to the mitochondrial surface where it constricts mitochondrial tubules. Fusion of the outer membranes is catalyzed by mitofusin 1 and 2 (MFN1, MFN2), whereas fusion of the mitochondrial inner membranes is catalyzed by the mitochondrial dynamin-like GTPase optic atrophy 1 (OPA1). Due to RNA splicing and protein processing, different isoforms of OPA1 exist. The long isoforms localize to the mitochondrial inner membrane through their transmembrane domains, whereas the short isoforms are expressed as soluble proteins in the mitochondrial intermembrane space. A balance of long and short OPA1 isoforms is required to maintain a healthy mitochondrial network (Del Dotto et al., 2017; MacVicar and Langer, 2016).

OPA1 is crucial for tissue development. *Opa1* heterozygous animals are viable, but experience a progressive loss of retinal ganglion cells (RGCs), optic nerve degeneration, and abnormal brain development (Davies et al., 2007; Alavi et al., 2007), whereas *Opa1*-null mice die early during embryonic development due to growth retardation and morphological abnormalities (Davies et al., 2007; Alavi et al., 2007). In humans, heterozygous mutations in *OPA1* cause the most common form of autosomal dominant optic atrophy (ADOA), a neuropathy wherein the majority of patients experience impaired vision (Delettre et al., 2000; Alexander et al., 2000). Homozygous mutations in *OPA1* result in severe and fatal infantile disorders with neurodevelopmental deficits, multi-organ complications, encephalopathy, cardiomyopathy, and optic atrophy (Spiegel et al., 2016; Nasca et al., 2017).

To elucidate the molecular mechanisms by which OPA1 contributes to human neural development, we used *OPA1* haploinsufficient pluripotent stem cell lines and differentiated them into neural progenitor cells

[1]Centre for Molecular Medicine Norway, Nordic EMBL Partnership, University of Oslo and Oslo University Hospital, 0318 Oslo, Norway

[2]GliaLab and Letten Centre, Division of Physiology, Department of Molecular Medicine, Institute of Basic Medical Sciences, University of Oslo, 0317 Oslo, Norway

[3]Laboratory of Clinical Biochemistry and Metabolism, Department of General Pediatrics, Adolescent Medicine and Neonatology, Faculty of Medicine, Medical Center, University of Freiburg, Mathildenstraße 1, 79106 Freiburg, Germany

[4]Ludwig Institute for Cancer Research Brussels, 1200 Brussels, Belgium

[5]Université Catholique de Louvain and de Duve Institute, 1200 Brussels, Belgium

[6]Department of Molecular Cell Biology, Institute for Cancer Research, Oslo University Hospital, 0424 Oslo, Norway

[7]Department of Pathology, Oslo University Hospital, 0424 Oslo, Norway

[8]Department of Ophthalmology, Cliniques Universitaires Saint-Luc, UCL, 1200 Brussels, Belgium

[9]Department for Cancer Immunology, Institute for Cancer Research, Oslo University Hospital, 0424 Oslo, Norway

[10]Institute of Clinical Medicine, University of Oslo, 0318 Oslo, Norway

[11]Department of Haematology, Oslo University Hospital, 0424 Oslo, Norway

[12]Lead Contact

*Correspondence: judith.staerk@ncmm.uio.no

https://doi.org/10.1016/j.isci.2020.101154

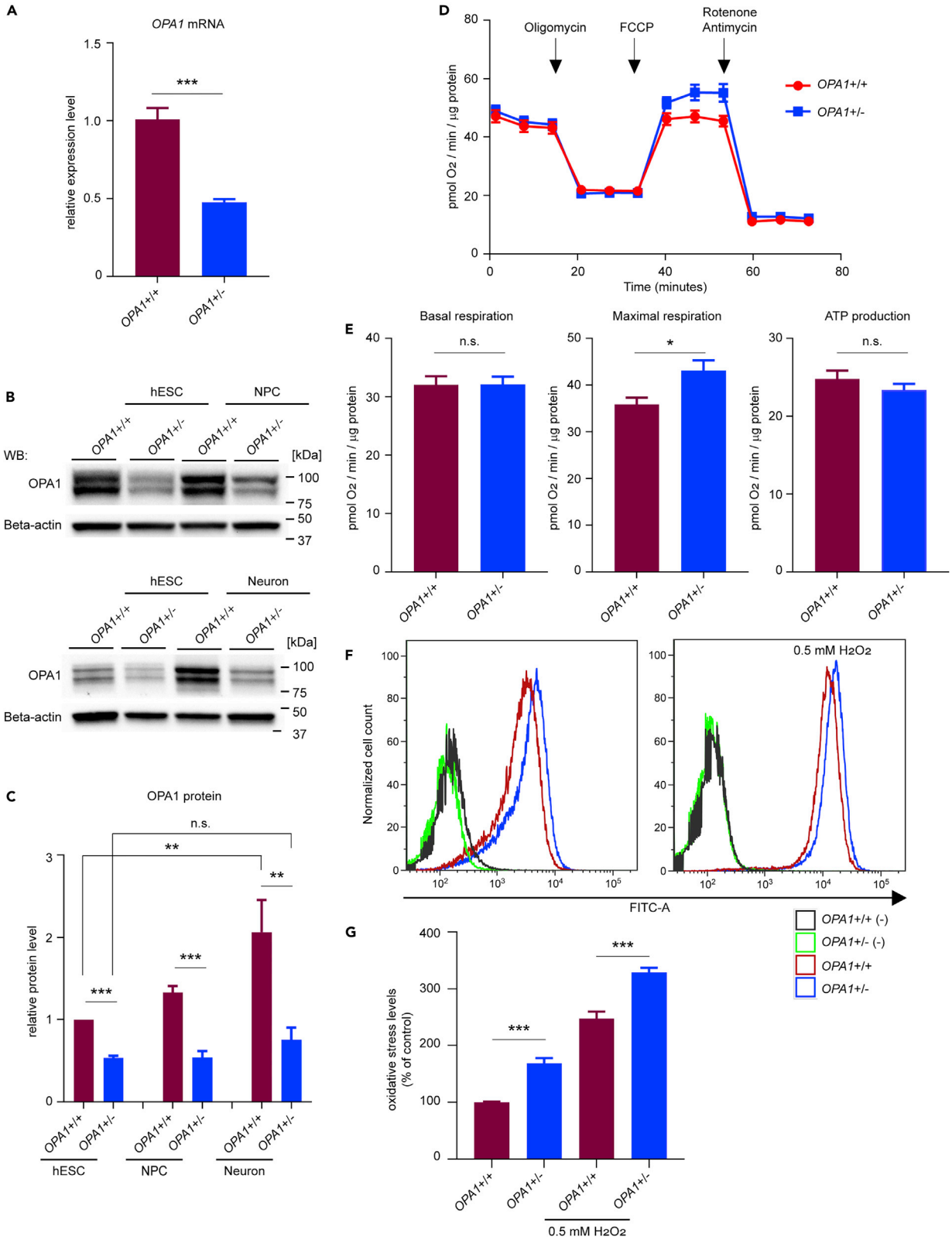
A
OPA1 mRNA
relative expression level
1.5
1.0
0.5
0
***
OPA1+/+
OPA1+/-
B
hESC
NPC
WB:
OPA1+/+
OPA1+/-
OPA1+/+
OPA1+/-
[kDa]
OPA1
Beta-actin
100
75
50
37
hESC
Neuron
OPA1+/+
OPA1+/-
OPA1+/+
OPA1+/-
[kDa]
OPA1
Beta-actin
100
75
50
37
C
OPA1 protein
relative protein level
n.s.
**
**
***
***
3
2
1
0
OPA1+/+
OPA1+/-
OPA1+/+
OPA1+/-
OPA1+/+
OPA1+/-
hESC
NPC
Neuron
D
Oligomycin
FCCP
Rotenone
Antimycin
pmol O2 / min / µg protein
80
60
40
20
0
0
20
40
60
80
Time (minutes)
OPA1+/+
OPA1+/-
E
Basal respiration
Maximal respiration
ATP production
pmol O2 / min / µg protein
40
30
20
10
0
n.s.
50
40
30
20
10
0
*
30
20
10
0
n.s.
OPA1+/+
OPA1+/-
OPA1+/+
OPA1+/-
OPA1+/+
OPA1+/-
F
Normalized cell count
100
80
60
40
20
0
10²
10³
10⁴
10⁵
0.5 mM H2O2
FITC-A
OPA1+/+ (-)
OPA1+/- (-)
OPA1+/+
OPA1+/-
G
oxidative stress levels
(% of control)
400
300
200
100
0
***
***
OPA1+/+
OPA1+/-
OPA1+/+
OPA1+/-
0.5 mM H2O2

Figure 1. *OPA1* Haploinsufficiency Induces Oxidative Stress in hESCs

(A) *OPA1* mRNA expression levels in hESCs determined by qRT-PCR analysis.

(B) Representative immunoblotting images showing OPA1 protein levels in hESCs, week 3 NPCs, and neurons. Beta-actin was used as loading control.

(C) Densitometric analysis of immunoblots in *OPA1+/+* and *OPA1+/−* cells. Mean ± SEM, N = 4 independent experiments.

(D) Oxygen consumption rate changes under mitochondrial stress in *OPA1+/+* and *OPA1+/−* hESCs. Oligomycin, FCCP, antimycin, and rotenone were sequentially applied. Mean ± SEM, N = 2 independent experiments.

(E) Basal respiration rates, maximum respiration rates, and ATP production calculated in *OPA1+/+* and *OPA1+/−* hESCs. Mean ± SEM, N = 2 independent experiments were performed and N ≥ 9 technical replicates were analyzed for each genotype. Student's t test was used to analyze the difference between two groups. n.s. not significant. *$p < 0.05$.

(F) Representative flow cytometry analysis of *OPA1+/+* and *OPA1+/−* hESCs labeled with the hydrogen peroxide-sensitive oxidative stress indicator CM-H2DCFDA. Unlabeled hESCs (−) were used as negative control. hESCs that were incubated with 0.5 mM H_2O_2 were used as positive control.

(G) Quantification of flow cytometry measurements in *OPA1+/+* and *OPA1+/−* hESCs. Arithmetic mean values were normalized to the values of labeled *OPA1+/+* hESCs.

Mean ± SEM, N ≥ 3 independent experiments and N = 2 technical replicates. Student's t test was used to analyze difference between two groups. n.s. not significant. **$p < 0.01$, ***$p < 0.001$. See also Figures S1, S2, and S4.

(NPCs) and forebrain neurons. Although we were able to generate NPCs and glutamatergic neurons, *OPA1* haploinsufficiency interfered with GABAergic interneuron formation. We then explored the molecular changes associated with the observed altered neural cell specification and identified a novel function for OPA1.

RESULTS

OPA1 Haploinsufficiency Induces Oxidative Stress in hESCs

To study the role of OPA1 during neural development, we used human embryonic stem cells (hESCs) and the CRISPR-Cas9 gene editing technology and deleted a stretch of nucleotides, which induces a frame-shift and a premature stop codon in the second exon of the *OPA1* transcript (Figure S1A). Because the majority of human disorders linked to *OPA1* are caused by heterozygous mutations, we targeted one allele only. We found a 50% reduction in *OPA1* mRNA transcript levels in heterozygous *OPA1+/−* compared with *OPA1+/+* hESCs, confirming that only one *OPA1* allele was transcribed (Figure 1A). The reduction in mRNA expression levels correlated with a 50% reduction in OPA1 protein levels in hESCs, indicating a non-sense-mediated RNA decay in *OPA1+/−* cells (Figures 1B and 1C). Expression levels of OCT4 and NANOG were comparable between *OPA1+/−* and parental hESCs, as shown by immunostaining and immunoblotting (Figures S1B and S1C). Moreover, hESC proliferation rates, assessed by automated live-cell analysis system, were similar between the two genotypes (Figure S1D). To further analyze cell cycle dynamics in *OPA1+/−* hESCs, we performed flow cytometry (fluorescence-activated cell sorting [FACS]) analysis of hESCs labeled with the fluorescent DNA-intercalating dye propidium iodide (PI) and Ki-67 antibody. The ratio of cells in G0/G1, S, and G2/M phases (Figures S1E and S1F), as well as Ki-67 labeling (Figure S1G), were similar between *OPA1+/+* and *OPA1+/−* hESC, indicating that *OPA1* haploinsufficiency does not affect pluripotency or proliferation rates in hESCs. Using transmission electron microscopy (TEM), we then assessed mitochondrial morphology and distribution in *OPA1+/−* hESCs. The TEM images showed no obvious differences in mitochondrial morphology between *OPA1+/+* and *OPA1+/−* hESCs (Figure S2A). Next, we measured mitochondrial length in *OPA1+/+* and *OPA1+/−* hESCs and binned the data into categories of intervals. Although this analysis revealed no significant change, we found a trend of more fragmented mitochondria in *OPA1+/−* hESCs (Figure S2B). We therefore determined the circumference of mitochondria, and found a small, but significant decrease in circumference in *OPA1+/−* compared with *OPA1+/+* hESCs (Figure S2C). In addition, we found a significant increase in the intercristae distance in *OPA1+/−* compared with *OPA1+/+* hESCs (Figures S2D and S2E). Mitochondria-targeted GFP (mito-GFP)-transduced hESCs also demonstrated that there was no obvious difference in mitochondrial shape or size among the two genotypes (Figure S2F). The mitochondrial DNA content, as analyzed by copy number of the mitochondrial genes NADH-ubiquinone oxidoreductase chain 1 (*MT-ND1*) and *MT-ND4,* was similar between *OPA1+/+* and *OPA1+/−* hESCs (Figure S2G). Using mitochondrial respiration assays, we found similar ATP production and basal respiration rates (Figures 1D and 1E) and an increase in maximal respiration in *OPA1+/−* compared with *OPA1+/+* hESCs (Figures 1D and 1E). Next, we analyzed whether reactive oxygen species (ROS) were altered in *OPA1+/−* hESCs. Flow cytometry analysis using the hydrogen peroxide-sensitive ROS indicator CM-H2DCFDA revealed significantly increased ROS levels in *OPA1+/−* compared with *OPA1+/+* hESCs (Figures 1F and 1G). Taken together, our results reveal subtle changes in the mitochondrial morphology and increased levels of ROS in *OPA1* haploinsufficient hESCs.

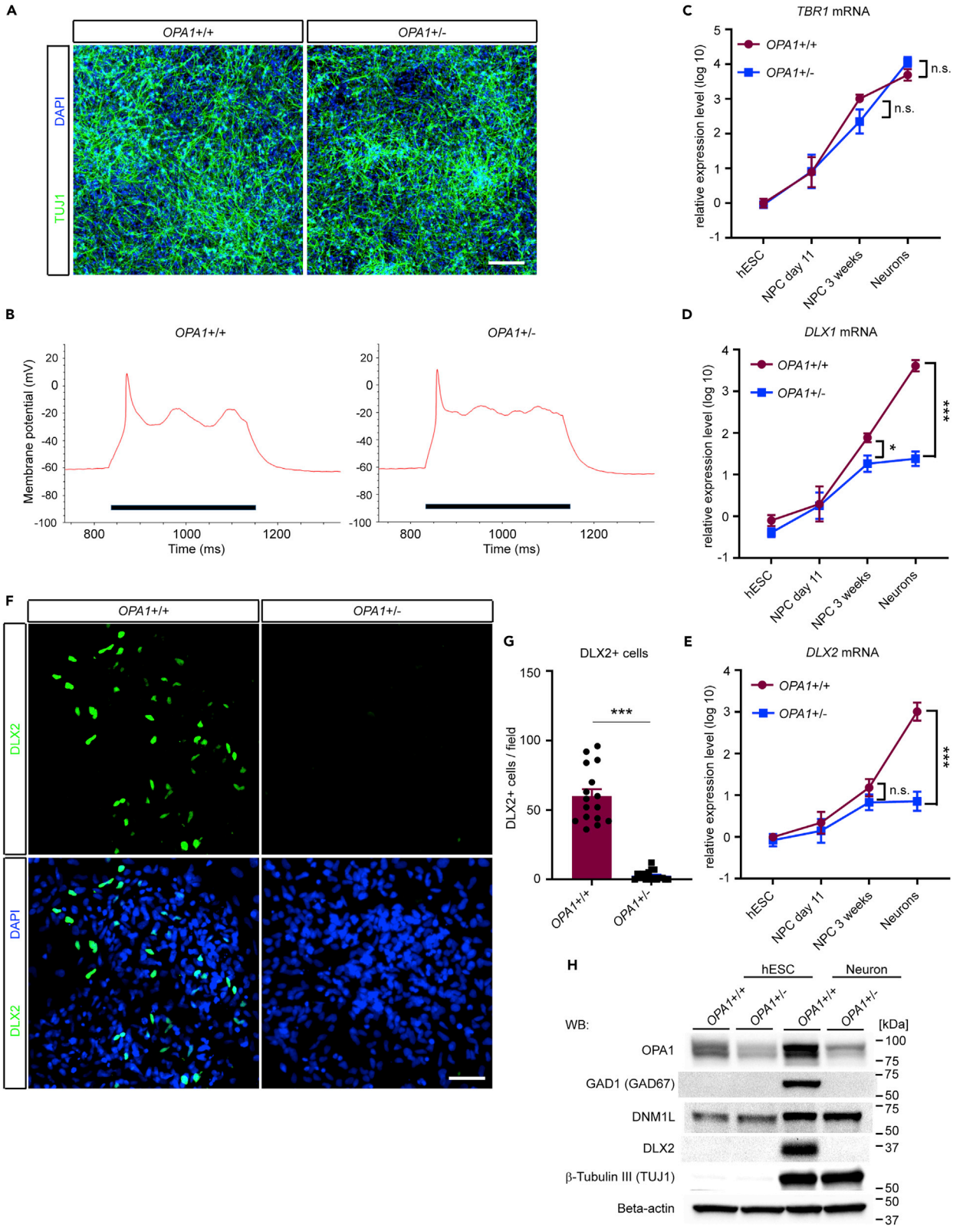
A
OPA1+/+
OPA1+/-
DAPI
TUJ1
B
OPA1+/+
OPA1+/-
Membrane potential (mV)
Time (ms)
C
TBR1 mRNA
relative expression level (log 10)
n.s.
hESC
NPC day 11
NPC 3 weeks
Neurons
D
DLX1 mRNA
*
***
E
DLX2 mRNA
F
DLX2
G
DLX2+ cells
DLX2+ cells / field
H
hESC
Neuron
WB:
[kDa]
OPA1
GAD1 (GAD67)
DNM1L
DLX2
β-Tubulin III (TUJ1)
Beta-actin

Figure 2. *OPA1* Heterozygous NPCs Fail to Generate DLX1/2+ Neurons

(A) Beta-tubulin III (TUJ1) staining of neurons. Scale bar, 100 μm.

(B) Representative traces of patch-clamped neurons. Action potentials were elicited in *OPA1*+/+ and *OPA1*+/− neurons upon depolarizing current injection. Black bar indicates time of depolarizing current injection.

(C–E) (C) *TBR1*, (D) *DLX1*, and (E) *DLX2* mRNA levels determined by qRT-PCR analyses in *OPA1*+/+ and *OPA1*+/− hESCs, NPCs, and neurons. Mean ± SEM, N ≥ 3 independent experiments for each genotype and cell type.

(F) Immunostaining images of *OPA1*+/+ and *OPA1*+/− neurons. DAPI was used to stain nuclei. Scale bar, 100 μm.

(G) Quantification of DLX2+ neurons. Mean ± SEM, N = 3 independent experiments.

(H) Immunoblotting showing OPA1, DNM1L, GAD1/GAD67, DLX2, and beta-tubulin III protein expression in *OPA1*+/+ and *OPA1*+/− hESCs and neurons. Beta-actin was used as loading control.

Student's t test was used to analyze difference between two groups. n.s. not significant. *$p < 0.05$, ***$p < 0.001$. See also Figures S3 and S4.

OPA1 Expression Is Upregulated during Neural Differentiation

Next, we investigated how *OPA1* heterozygosity affects neural differentiation. Using the dual SMAD inhibition protocol (Chambers et al., 2009; Shi et al., 2012), hESCs were differentiated into neuroepithelial progenitors and NPCs (Figure S3A). On day 11 of the differentiation protocol, neural commitment was evident by morphological transformation and expression of the neural stem cell marker PAX6 (day 11 NPCs, Figure S3B). After passaging and further differentiation, PAX6-positive NPCs reorganized themselves into neural rosette structures (week 3 NPCs, Figure S3C) before being differentiated into beta-tubulin III-positive neurons (Figure S3D). To assess the neurogenic ability of hESCs, we first compared rosette formation of NPCs. Immunostainings showed that *OPA1*+/− NPCs formed tight junction protein Zonula-occludens-1 (ZO-1)-positive rosette structures with comparable efficiency as *OPA1*+/+ cells (Figure S3E). As the self-organization of neural rosettes is reminiscent of neural tube formation from neuroepithelium (Deglincerti et al., 2016), these results reveal that early neural development is not affected by *OPA1* haploinsufficiency.

Quantification of *OPA1* transcript levels by qRT-PCR showed a 25% increase of total *OPA1* mRNA levels during neuronal differentiation (Figure S4A). *OPA1* is alternatively spliced in different tissues. Of these splice variants, *OPA1* transcript variant 1 (NM_015560), which lacks exons 4b and 5b (Figure S1A), is the most abundantly expressed isoform in the mouse brain and retina (Delettre et al., 2001; Akepati et al., 2008). In line with this, we found that *OPA1* isoform 1 levels markedly increased in our neuronal cultures (Figure S4B). Moreover, we found that isoform 1 became the predominant splice form during neural differentiation. In hESCs, the ratio of transcript variant 1 to total *OPA1* mRNA levels was approximately 1:1, whereas in neurons the majority of *OPA1* transcripts were isoform 1 (Figure S4C). Immunoblotting experiments showed a 25% and 2-fold increase of OPA1 protein in *OPA1*+/+ NPCs and neurons when compared with hESCs, respectively (Figures 1B, 1C, and S4D).

OPA1 Heterozygous NPCs Fail to Generate DLX1/2+ Neurons

To investigate the role of OPA1 during differentiation and neuronal function further, we analyzed neurons derived from *OPA1*+/+ and *OPA1*+/− NPCs. Immunostaining experiments showed that pan-neuronal marker beta-tubulin III-positive neurons could be efficiently generated from both genotypes, indicating that *OPA1* haploinsufficiency is not affecting overall neuronal development (Figure 2A). Patch-clamp experiments demonstrated that *OPA1* haploinsufficiency did not interfere with the ability of neurons to fire action potentials in response to current stimuli (Figure 2B). To determine neuronal lineage specification, we selected T-box brain 1 (*TBR1*) as a marker for glutamatergic neurons (Hevner et al., 2001), and *DLX1* and *DLX2* as they are important for specification of RGCs and GABAergic neurons (Anderson et al., 1997; Letinic et al., 2002; de Melo et al., 2005). As expected, *TBR1*, *DLX1*, and *DLX2* mRNA expression levels increased during the neuronal differentiation of *OPA1*+/+ hESCs (Figures 2C–2E), demonstrating that our neuronal cultures included cell types representing forebrain development. During neuronal differentiation of *OPA1*+/− hESCs, we found that *TBR1* was expressed at similar levels as in *OPA1*+/+ cells (Figure 2C). However, *OPA1*+/− cells notably failed to induce mRNA expression of *DLX1* and *DLX2* during neuronal maturation (Figures 2D and 2E). Using immunostaining, we showed that there were significantly less DLX2 immunoreactive cells in *OPA1*+/− compared with *OPA1*+/+ neuronal cultures (Figures 2F and 2G). The absence of DLX2 protein in lysates of *OPA1*+/− but not *OPA1*+/+ neurons was further confirmed using immunoblotting (Figure 2H). Neurons derived from both genotypes expressed comparable levels of beta-tubulin III protein (Figure 2H).

OPA1 Haploinsufficient NPCs Do Not Give Rise to GABAergic Interneurons

DLX1 and DLX2 are transcription factors (TFs) important for GABAergic interneuron and RGC development (Letinic et al., 2002; Anderson et al., 1997; de Melo et al., 2005). As their downregulation indicated

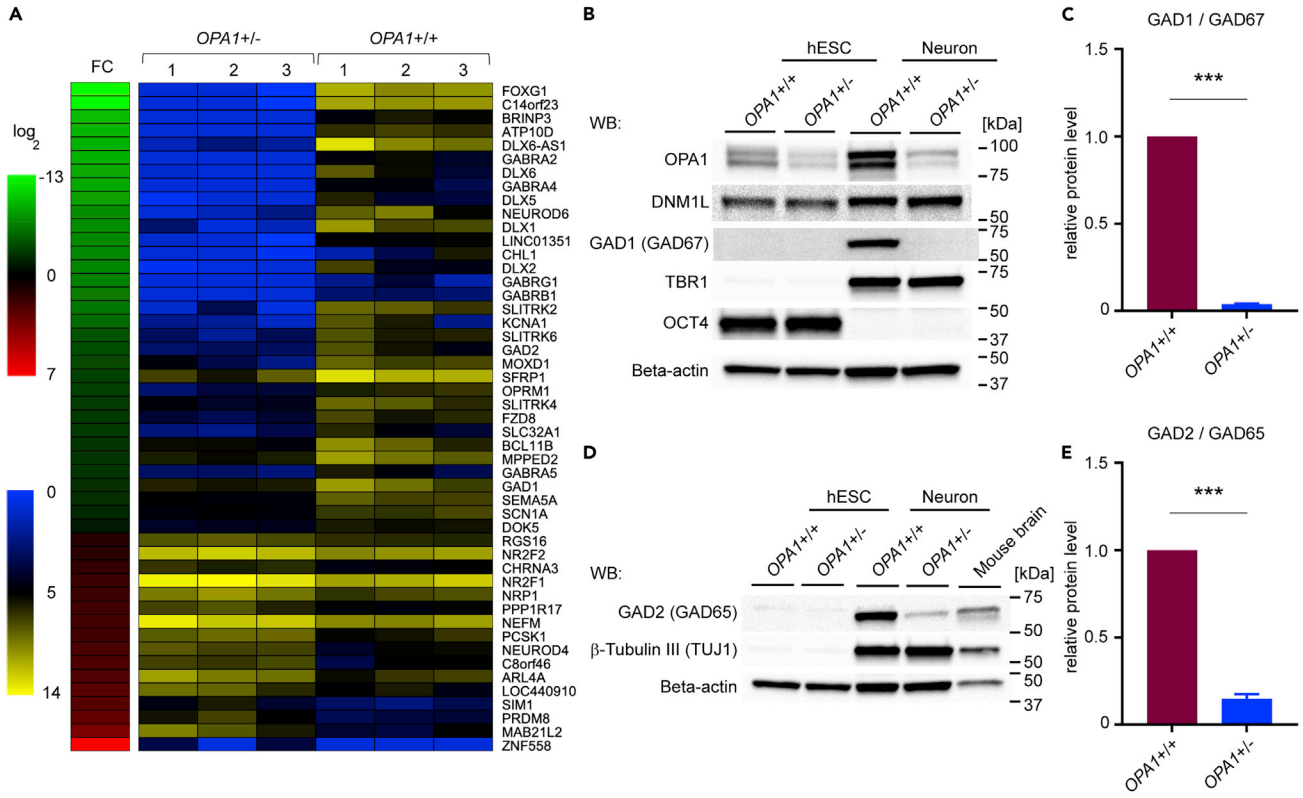

Figure 3. *OPA1* Haploinsufficient NPCs Do Not Give Rise to GABAergic Interneurons

(A) Log_2 fold-change and expression heatmaps of selected down- (green) and up- (red) regulated genes in *OPA1*+/− compared with *OPA1*+/+ neurons. FC = fold-change. Expression intensities are displayed from blue (low expression) to yellow (high expression).

(B) Immunoblotting showing OPA1, DNM1L, TBR1, and GAD1/GAD67 protein expression in *OPA1*+/+ and *OPA1*+/− hESCs and neurons. OCT4 was used as pluripotency marker; beta-actin was used as loading control.

(C) Densitometric analysis of GAD1 protein levels in *OPA1*+/+ and *OPA1*+/− neurons. Mean ± SEM, N = 2 independent experiments.

(D) Immunoblotting showing GAD2/GAD65 and beta-tubulin III protein expression in *OPA1*+/+ and *OPA1*+/− hESCs and neurons.

(E) Densitometric analysis of GAD2 protein levels in *OPA1*+/+ and *OPA1*+/− neurons. Mean ± SEM, N = 2 independent experiments.

Student's t test was used to analyze difference between two groups. ***$p < 0.001$. See also Figures S3 and S4, and Table S1.

an altered neuronal function and differentiation potential when *OPA1* was reduced, we performed RNA sequencing (RNA-seq) in 7-week-old neurons. We found several genes encoding for TFs with known function in neurogenesis differentially regulated in *OPA1*+/− neurons (Table S1). For instance, *FOXG1*, *DLX1*, *DLX2*, *DLX5*, and *DLX6* were genes highly downregulated in *OPA1*+/− compared with *OPA1*+/+ neurons (Figure 3A; Table S1). Moreover, expression of *SFRP1* and *SEMA5A*, which are known to control RGC development and axonal growth, as well as *CTIP2/BCL11B* and *NEUROD6*, which are TFs that are highly expressed in the developing brain and retinal cells (Cherry et al., 2011), were also significantly downregulated. Other genes downregulated included *SLITRK2*, *SLITRK4*, and *SLITRK6*, which are plasma membrane proteins expressed in the retina, and several GABA receptor subunits (*GABRA2*, *GABRA4*, *GABRB1*, and *GABRG1*). Among the upregulated genes in *OPA1*+/− neurons we found *NR2F1*, *NR2F2*, and *NEUROD4*, which are TFs known to regulate cell fate specification in the retina (Figure 3A).

The absence of DLX1/2 expression in *OPA1*+/− neurons prompted us to further investigate GABAergic neuronal markers. Glutamate decarboxylase 1 (GAD1/GAD67) and 2 (GAD2/GAD65), which catalyze the production of GABA from L-glutamic acid, were expressed in *OPA1*+/+ neurons, whereas they were absent or markedly reduced in *OPA1*+/− neurons (Figures 3B–3E and S4E). TBR1 and beta-tubulin III were expressed at comparable levels (Figures 3B and 3D). Overall, our transcriptional analysis demonstrates that reduced OPA1 protein levels alter the expression of genes that are important for GABAergic interneuron formation and retinal development.

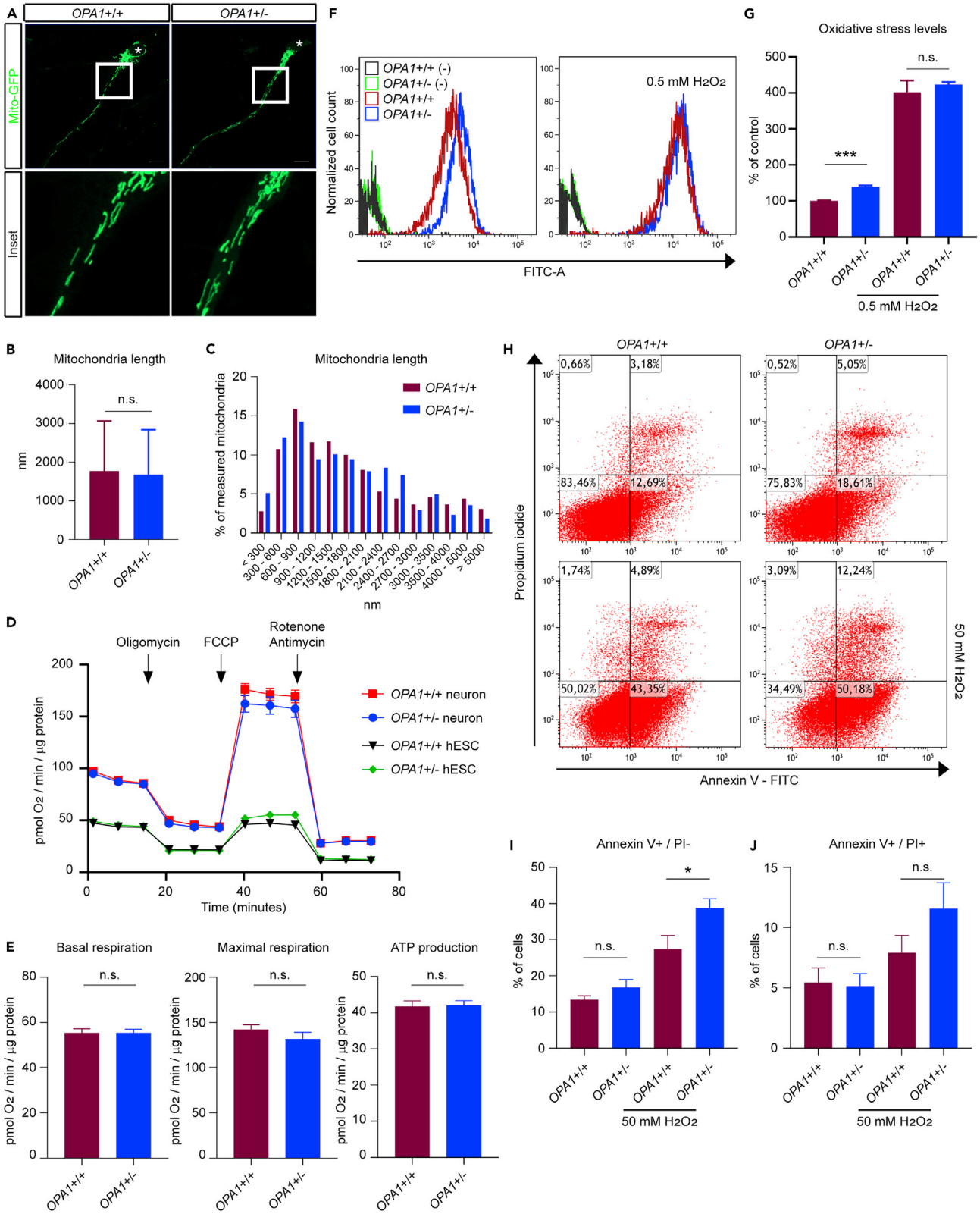
A
OPA1+/+
OPA1+/-
Mito-GFP
Inset
F
OPA1+/+ (-)
OPA1+/- (-)
OPA1+/+
OPA1+/-
0.5 mM H2O2
Normalized cell count
FITC-A
G
Oxidative stress levels
% of control
n.s.
***
0.5 mM H2O2
B
Mitochondria length
nm
n.s.
C
Mitochondria length
% of measured mitochondria
nm
H
Propidium iodide
Annexin V - FITC
50 mM H2O2
0,66%
3,18%
83,46%
12,69%
0,52%
5,05%
75,83%
18,61%
1,74%
4,89%
50,02%
43,35%
3,09%
12,24%
34,49%
50,18%
D
Oligomycin
FCCP
Rotenone
Antimycin
pmol O2 / min / µg protein
Time (minutes)
OPA1+/+ neuron
OPA1+/- neuron
OPA1+/+ hESC
OPA1+/- hESC
I
Annexin V+ / PI-
% of cells
J
Annexin V+ / PI+
E
Basal respiration
Maximal respiration
ATP production

Figure 4. *OPA1* Haploinsufficiency Induces Oxidative Stress and Apoptosis in Neurons

(A) Confocal microscopic images of mito-GFP-transduced *OPA1*+/+ and *OPA1*+/− neurons. * denotes nucleus. Scale bar, 10 μm.

(B) Quantification of mitochondria length in *OPA1*+/+ and *OPA1*+/− neurons. N = 680 mitochondria for *OPA1*+/+ and N = 645 mitochondria for *OPA1*+/− were measured.

(C) Mitochondrial length was measured and binned into categories of length intervals.

(D) Oxygen consumption rate changes under mitochondrial stress in *OPA1*+/+ and *OPA1*+/− neurons. Oligomycin, FCCP, antimycin, and rotenone were sequentially applied. Mean ± SEM, N = 2 independent experiments.

(E) Basal respiration rates, maximum respiration rates, and ATP production calculated in *OPA1*+/+ and *OPA1*+/− neurons. Mean ± SEM, N = 2 independent experiments were performed and N ≥ 40 technical replicates were analyzed for each genotype.

(F) Representative flow cytometry analysis of *OPA1*+/+ and *OPA1*+/− neurons labeled with the hydrogen peroxide-sensitive oxidative stress indicator CM-H2DCFDA. Unlabeled neurons (−) were used as negative control. Neurons that were incubated with 0.5 mM H_2O_2 were used as positive control.

(G) Quantification of flow cytometry measurements in *OPA1*+/+ and *OPA1*+/− neurons. Arithmetic mean values were normalized to the values of labeled *OPA1*+/+ neurons. Mean ± SEM, N ≥ 3 independent experiments and N = 2 technical replicates.

(H) Representative flow cytometry analysis of live *OPA1*+/+ and *OPA1*+/− neurons labeled with the early apoptosis indicator annexin V and late-apoptosis indicator propidium iodide (PI). Neurons were incubated with 50 mM H_2O_2 to assess sensitivity to apoptotic stimuli.

(I) Quantification of early apoptotic annexin V+/PI− neurons. Percentage of labeled cells in total gated cells is shown.

(J) Quantification of late-apoptotic Annexin V+/PI+ neurons. Percentage of labeled cells in total gated cells is shown.

Mean ± SEM, N = 4 independent experiments and N = 2 technical replicates. Student's t test was used to analyze difference between two groups. n.s. not significant. *$p < 0.05$, *** $p < 0.001$. See also Figures S3 and S4.

We imaged mito-GFP-transduced neurons to assess mitochondrial morphology. Confocal microscopy analysis demonstrated that mitochondrial morphology and distribution were similar in *OPA1*+/− and *OPA1*+/+ neurons (Figure 4A). Quantification of mitochondrial length and binning of measurements into categories of intervals showed no evident differences in mitochondrial distribution (Figures 4B and 4C). Next, we analyzed energy metabolism in *OPA1*+/− and *OPA1*+/+ neuronal cultures using mitochondrial respiration assays. Our data revealed that neurons exhibited an increased mitochondrial respiration compared with hESCs (Figure 4D). However, basal respiration, maximal respiration, and ATP production rates were similar in *OPA1*+/− and *OPA1*+/+ neurons (Figure 4E), suggesting that *OPA1* haploinsufficiency does not affect mitochondrial respiration in neurons. We then investigated oxidative stress levels in neuronal cultures. Flow cytometry analysis showed significantly increased ROS levels in *OPA1*+/− compared with *OPA1*+/+ neurons (Figures 4F and 4G). FACS analysis of neurons labeled with the early apoptosis indicator Annexin V and late apoptosis indicator PI (Figure 4H) demonstrated no differences in apoptosis in neuronal culture conditions (Figures 4I and 4J). Importantly, when neurons were exposed to stress by pre-treatment with hydrogen peroxide we observed significantly more Annexin V+ cells in *OPA1*+/− compared with *OPA1*+/+ neurons (Figures 4I and 4J).

OPA1 Heterozygous NPCs Exhibit a Significantly Altered Transcriptional Signature

Next, we addressed whether the impaired formation of DLX1/2+ neurons in *OPA1*+/− cultures could be explained by an altered transcriptional circuitry at the NPC level. Successful formation of day 11 NPCs was verified by the loss of the pluripotency markers OCT4 and NANOG, and the gain of the neural stem cell marker PAX6 (Figure S5A). We then performed RNA-seq analysis in *OPA1*+/+ and *OPA1*+/− NPCs after 11 days and 3 weeks of differentiation to elucidate potential transcriptional changes associated with *OPA1* haploinsufficiency. Principal-component analysis was used to assess and visualize the neural differentiation trajectory (Figure 5A). When we analyzed differentially expressed genes (DEGs) at day 11 *OPA1*+/− versus *OPA1*+/+ NPCs, we found *FOXG1* already highly downregulated at this early NPC stage (Figure 5B and Table S2). Another gene we found highly downregulated encodes for TAF9B (Figure 5B and Table S2), a protein that is part of the neuronal core promoter complex and known to regulate the induction of specific neuronal genes (Herrera et al., 2014). Moreover, we found *SLITRK2*, a transmembrane protein expressed in proliferative neuroblastic layer of the retina (Beaubien and Cloutier, 2009), to be significantly downregulated in *OPA1*+/− NPCs (Figure 5B and Table S2). In addition, *GABRA2*, the gene coding for GABRA receptor alpha 2; *ATP10D*, a putative phospholipid transporting ATPase; and several neural cell adhesion genes, including *NCAM2*, *PCDHGA3*, and *PCDHGA6*, were also downregulated (Figure 5B and Table S2). Significantly upregulated genes in day 11 *OPA1*+/− versus *OPA1*+/+ NPCs included genes coding for neural guidance proteins, such as *SEMA3E*, *SLIT3*, Ephrin type-A receptor 1 (*EPHA1*), and its ligand ephrin A1 (*EFNA1*) (Figure 5B and Table S2).

DEG analysis of *OPA1*+/− compared with *OPA1*+/+ NPCs in week 3 revealed that *FOXG1*, *ATP10D*, *GABRA2*, *SLITRK2*, *ZNF280D*, and *TAF9B* also remained highly downregulated at this later stage of differentiation (Figure S5B and Table S3). In addition, several genes encoding for TFs involved in primary

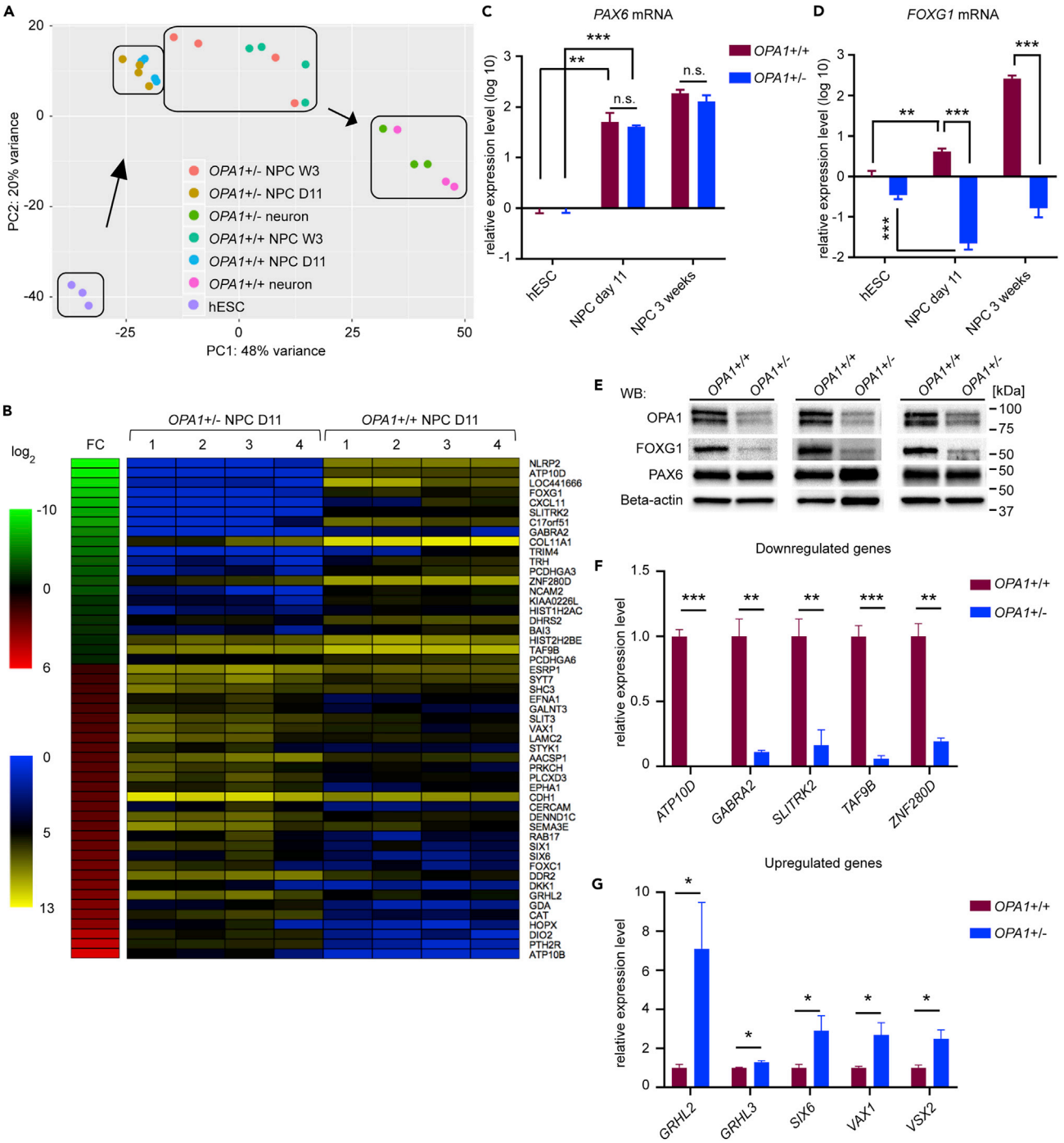

Figure 5. *OPA1* Haploinsufficiency Significantly Alters the Transcriptional Circuitry in NPCs

(A) Principal-component analysis of hESCs, day 11 and week 3 NPCs, and neurons.

(B) Log_2 fold-change and expression heatmaps of selected down- (green) and up- (red) regulated genes in *OPA1+/−* compared with *OPA1+/+* day 11 NPCs. FC = fold-change. Expression intensities are displayed from blue (low expression) to yellow (high expression).

(C and D) (C) *PAX6* and (D) *FOXG1* mRNA levels in day 11 and week 3 NPCs, normalized to transcript levels in *OPA1+/+* hESCs.

(E) Immunoblotting showing OPA1, FOXG1, and PAX6 protein expression in NPCs. Beta-actin was used as loading control. N = 3 independent experiments.

(F) *ATP10D*, *GABRA2*, *SLITRK2*, *TAF9B*, and *ZNF280D* mRNA expression levels in day 11 NPCs. mRNA expression levels were normalized to transcript levels in *OPA1+/+* NPCs.

Figure 5. *Continued*

(G) *GRHL2*, *GRHL3*, *SIX6*, *VAX1*, and *VSX2* mRNA expression levels in day 11 NPCs. mRNA expression levels were normalized to transcript levels in *OPA1*+/+ NPCs.

Mean ± SEM, N ≥ 4 independent samples for each genotype and cell type. Student's t test was used to analyze the differences between two groups. n.s. not significant. *p < 0.05, **p < 0.01, ***p < 0.001. See also Figures S3, S5, and S6, and Tables S2 and S3.

neurulation, forebrain development, and retinal development were upregulated in *OPA1*+/− NPCs. These included *SIX6*, *GRHL2*, *GRHL3*, *VAX1*, and *VSX2* (Figure S5B and Table S3). Overall, our RNA-seq analyses identified significant alterations in the transcriptional circuitry of *OPA1*+/− NPCs (Figures 5B and S5B, Tables S2 and S3), which can explain the observed altered neuronal cell fate specification.

We then assessed the expression levels of selected genes in more detail. qRT-PCR analysis at three different time points showed continuous increase of *PAX6* mRNA expression levels during NPC derivation (Figure 5C). *OPA1*+/+ NPCs also showed significant upregulation of *FOXG1*, starting 11 days after differentiation (Figure 5D), a finding in line with its previously described critical role in early brain development (Xuan et al., 1995). *OPA1*+/− NPCs expressed similar *PAX6* mRNA levels as *OPA1*+/+ NPCs (Figure 5C), whereas *FOXG1* transcription was absent in *OPA1*+/− cells during all stages of NPC differentiation (Figure 5D). This was also true at the protein level (Figure 5E). In addition, we used qRT-PCR analyses to confirm the downregulation of *ATP10*, *GABRA2*, *SLITRK2*, *TAF9B*, and *ZNF280D* (Figure 5F) and upregulation of *GRHL2*, *GRHL3*, *SIX6*, *VAX1*, and *VSX2* mRNA expression in *OPA1*+/− compared with *OPA1*+/+ NPCs (Figure 5G). Using a second, independently derived *OPA1*+/− hESC clone #63, we confirmed reduced OPA1 protein (Figure S6A) and *OPA1* mRNA expression levels in *OPA1*+/− compared with *OPA1*+/+ hESC and NPCs, respectively. Moreover, *PAX6* mRNA expression was comparable between genotypes (Figure S6B), whereas *FOXG1* and *TAF9B* mRNA expression levels were also markedly reduced in *OPA1*+/− #63 NPCs (Figure S6B).

To investigate whether altered transcriptional regulation affects proliferation or cell survival of *OPA1*+/− NPCs, we performed FACS analysis of NPCs labeled with PI. Figures S5C and S5D showed no differences in cell cycle dynamics in *OPA1*+/+ and *OPA1*+/− NPCs. Similarly, Ki-67 expression was also comparable between the two genotypes (Figure S5E). Next, we analyzed the levels of apoptosis in NPCs under normal conditions and upon stimulation with hydrogen peroxide (Figure S5F). We found no significant difference in apoptosis between *OPA1*+/+ and *OPA1*+/− NPCs (Figure S5G), whereas pre-treatment of NPCs with hydrogen peroxide increased Annexin V+/PI+ late apoptotic cells in *OPA1*+/− NPCs (Figure S5H), supporting our results that *OPA1* haploinsufficiency increases the sensitivity of cells to apoptotic stimuli. Collectively, our data demonstrate that OPA1 is essential for proper transcriptional regulation in NPCs, and that *OPA1*+/− NPCs exhibit a developmental defect that causes impaired neural subtype specification.

OPA1 Protects against Aberrant DNA Methylation

Recently, it has been shown that metabolic stress and accumulation of mitochondria affect hematopoietic stem cell fate decisions through altered nuclear DNA methylation (Ho et al., 2017). Our transcriptome analyses showed that several genes important for NPC differentiation, GABAergic interneuron formation, and retinal development such as the pioneer transcription factor *FOXG1* were strongly downregulated in *OPA1*+/− NPCs. To address whether this downregulation was caused by epigenetic alterations, we analyzed the CpG content in annotated sequences and found CpG-enriched promoters in genes encoding *FOXG1*, *ATP10D*, *TAF9B*, *SLITRK2*, *GABRA2*, and *ZNF280D*. Figure 6A depicts the location and CpG-enriched regions in the promoter and 5′ UTR of *FOXG1*. Genomic DNA was isolated from NPCs, bisulfite treated, and the *FOXG1* 5′UTR region was sequenced. We found that all CpG bases within this region were methylated in *OPA1*+/− cells, whereas this was not the case in *OPA1*+/+ cells (Figure 6B). This result demonstrates that DNA hypermethylation was the reason for the observed repression of *FOXG1* transcription. The amplification of the *FOXG1* promoter CpG island was not possible due to the long CpG stretches, which prevented optimal primer design (Figure 6A). Bisulfite sequencing of the *ATP10D* locus also revealed a high content of methylated promoter CpG in *OPA1*+/− but not in *OPA1*+/+ NPCs (Figures 6C and 6D), further confirming that DNA methylation patterns were altered in *OPA1*+/− NPCs. Taken together, our results suggest that OPA1 is necessary for NPC transcriptional regulation by preventing aberrant methylation.

Next, we tested whether inhibition of DNA methylation can restore the transcriptional silencing in *OPA1*+/− NPCs. Strikingly, incubation of cells with the DNA methyltransferase (DNMT) inhibitor RG108 during

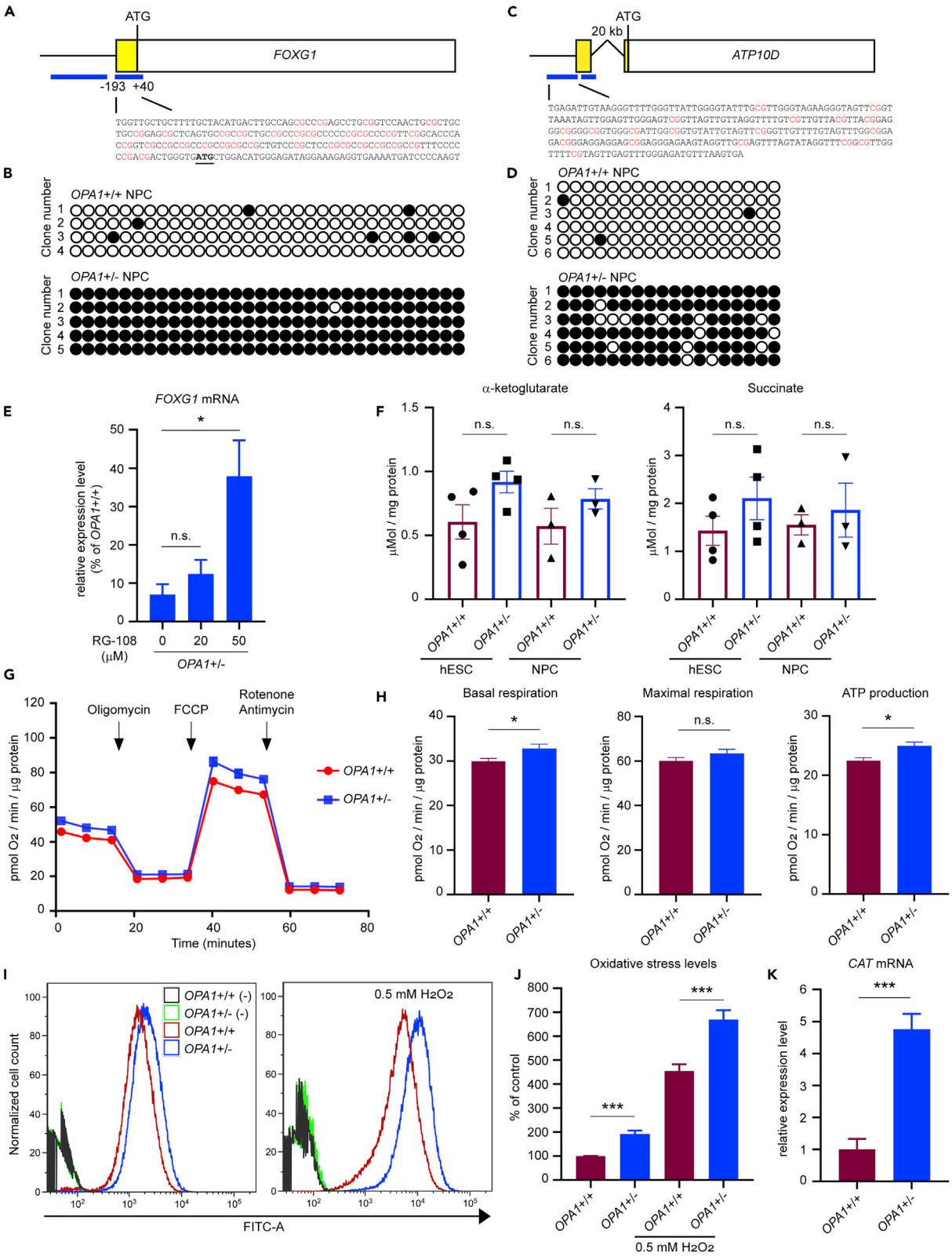
A
ATG
FOXG1
-193 +40
TGGTTGCTGCTTTTGCTACATGACTTGCCAGCGCCCGAGCCTGCGGTCCAACTGCGCTGC
TGCCGGAGCGCTCAGTGCCGCCGCTGCCGCCCGCGCCCCCCGCGCCCCGTTCGGCACCCA
CCGGTCGCCGCCGCCCGCCGCGCGCCGCTGTCCGCTCCCGCGCCGCGCCGCCGTTTCCCC
CCGACGACTGGGTGATGCTGGACATGGGAGATAGGAAAGAGGTGAAAATGATCCCCAAGT
B
OPA1+/+ NPC
OPA1+/- NPC
Clone number
C
ATG
20 kb
ATP10D
TGAGATTGTAAGGGTTTTGGGTTATTGGGGTATTTGCGTTGGGTAGAAGGGTAGTTCGGT
TAAATAGTTGGAGTTGGGAGTCGGTTAGTTGTTAGGTTTTGTCGTTGTTACGTTACGGAG
GGCGGGGCGGTGGGCGATTGGCGGTGTATTGTAGTTCGGGTTGTTTTGTAGTTTGGCGGA
GACGGGAGGAGGAGCGGAGGGAGAAGTAGGTTGCGAGTTTAGTATAGGTTTCGGCGTTGG
TTTTCGTAGTTGAGTTTGGGAGATGTTTAAGTGA
D
OPA1+/+ NPC
OPA1+/- NPC
Clone number
E
FOXG1 mRNA
relative expression level (% of OPA1+/+)
n.s.
*
RG-108 (μM)
0 20 50
OPA1+/-
F
α-ketoglutarate
Succinate
μMol / mg protein
n.s.
OPA1+/+ OPA1+/- OPA1+/+ OPA1+/-
hESC NPC
G
Oligomycin
FCCP
Rotenone Antimycin
OPA1+/+
OPA1+/-
pmol O2 / min / μg protein
Time (minutes)
H
Basal respiration
Maximal respiration
ATP production
pmol O2 / min / μg protein
n.s.
*
I
OPA1+/+ (-)
OPA1+/- (-)
OPA1+/+
OPA1+/-
0.5 mM H2O2
Normalized cell count
FITC-A
J
Oxidative stress levels
% of control
***
0.5 mM H2O2
K
CAT mRNA
relative expression level
***

Figure 6. OPA1 Protects against Aberrant DNA Methylation

(A) Location and sequence of CpG-enriched regions in the *FOXG1* gene promoter and 5′ UTR. ATG is indicated as translation start codon. Numbers denote sequences upstream (−) or downstream (+) of the start codon. The yellow box indicates the 5′ UTR, and blue lines represent CpG enriched regions. CpGs are marked in red.

(B) Bisulfite sequencing of the *FOXG1* 5′UTR in *OPA1*+/+ and *OPA1*+/− NPCs. Empty circles represent unmodified cytosines, and filled circles represent methylated cytosines.

(C) Location and sequence of CpG-enriched regions in the *ATP10D* gene promoter and 5′ UTR. ATG is indicated as translation start codon, and numbers denote sequences upstream (−) or downstream (+) of the start codon. Yellow box indicates the 5′ UTR flanked by a 20-kb intron, and blue lines represent CpG-enriched regions. CpGs are marked in red.

(D) Bisulfite sequencing of the *ATP10D* gene promoter in *OPA1*+/+ and *OPA1*+/− NPCs. Empty circles represent unmodified CpG bases, and filled circles represent methylated cytosines.

(E) *FOXG1* mRNA levels in day 11 *OPA1*+/− NPCs treated with different concentrations of DNMT inhibitor RG108. Mean ± SEM, N = 4 independent experiments with N = 2 technical replicates for each condition. mRNA expression levels were normalized to transcript levels in untreated *OPA1*+/+ NPCs.

(F) Succinate and alpha-ketoglutarate levels measured in *OPA1*+/+ and *OPA1*+/− hESCs and day 11 NPCs measured by mass spectrometry analysis. Mean ± SEM, N ≥ 3 independent samples for each genotype and cell type.

(G) Oxygen consumption rate changes under mitochondrial stress in *OPA1*+/+ and *OPA1*+/− NPCs. Oligomycin, FCCP, antimycin, and rotenone were sequentially applied. Mean ± SEM, N = 3 independent experiments.

(H) Basal respiration rates, maximum respiration rates, and ATP production in *OPA1*+/+ and *OPA1*+/− NPCs. Mean ± SEM, N = 3 independent experiments were performed and N ≥ 40 technical replicates were analyzed for each genotype.

(I) Representative flow cytometry analysis of *OPA1*+/+ and *OPA1*+/− NPCs labeled with the hydrogen peroxide-sensitive oxidative stress indicator CM-H2DCFDA. Unlabeled NPCs (−) were used as negative control. NPCs that were incubated with 0.5 mM H_2O_2 were used as positive control.

(J) Quantification of flow cytometry measurements in *OPA1*+/+ and *OPA1*+/− NPCs. Arithmetic mean values were normalized to the values of labeled *OPA1*+/+ NPCs. Mean ± SEM, N ≥ 4 independent experiments and N = 2 technical replicates.

(K) *CAT* mRNA expression levels in day 11 *OPA1*+/+ and *OPA1*+/− NPCs. mRNA expression levels were normalized to transcript levels in *OPA1*+/+ NPCs. Mean ± SEM, N ≥ 3 independent samples were assessed for each genotype. Student's t test was used to analyze the difference between two groups. n.s. not significant. *p < 0.05, ***p < 0.001. See also Figures S6 and S7.

neural differentiation resulted in a partial rescue of *FOXG1* expression in *OPA1*+/− NPCs, demonstrating that the transcriptional silencing caused by *OPA1* haploinsufficiency could be rescued by inhibiting DNMTs and preventing DNA methylation (Figure 6E). To determine whether DNA methylation and hydroxymethylation levels were affected on a global level in *OPA1*+/− NPCs, we used mass spectrometry-based quantification and found similar total methylation (5me(dC)) and hydroxymethylation (5hm(dC)) levels in *OPA1*+/+ and *OPA1*+/− NPCs (Figure S7A). Moreover, immunoblotting for DNMT3A and DNMT3B proteins showed similar expression levels between different genotypes, suggesting that reduced OPA1 levels lead to loci-specific rather than global DNA methylation changes (Figure S7B).

To further explore the potential cause for the observed loci-specific changes in DNA methylation, we analyzed the concentration of the small metabolites S-adenosylmethionine (SAM) and S-adenosylhomocysteine (SAH), which serve as substrates for DNMTs. Using mass spectrometry analysis we demonstrate that the overall SAM/SAH ratio in NPCs of both *OPA1*+/− and *OPA1*+/+ genotypes was significantly higher than in hESCs, indicating an overall higher methylation capacity in NPCs (Figure S7C). However, the overall SAM/SAH ratio was not altered when OPA1 was reduced (Figure S7C). Next, we quantified succinate and alpha-ketoglutarate levels in hESCs and NPCs. Again, there were no significant changes in succinate and alpha-ketoglutarate levels in *OPA1*+/− versus *OPA1*+/+ cells (Figure 6F), indicating that altered availability of these small metabolites is likely not the reason for the observed changes in DNA methylation.

When analyzing the mitochondrial energy metabolism in NPCs, we found a small but significant increase in basal respiration and ATP production levels in *OPA1*+/− compared with *OPA1*+/+ NPCs (Figures 6G and 6H). In addition, flow cytometry analysis showed significantly increased ROS levels in *OPA1*+/− NPCs (Figures 6I and 6J), further confirming our results in hESC and neurons. In line with the observed increased oxidative stress level in *OPA1*+/− NPCs, we found catalase (*CAT*) and *FOXC1* mRNA expression levels significantly upregulated in day 11 *OPA1*+/− NPCs (Figure 5B and Table S2). Catalase is a peroxisomal enzyme protecting cells against oxidative stress, and FOXC1 is a stress-responsive TF that provides resistance to oxidative stress in the eye (Mirzayans et al., 2007). The upregulation of *CAT* expression was confirmed by qRT-PCR in NPCs derived from two independent *OPA1*+/− lines (Figures 6K and S6B).

Patient-Derived iPSC Harboring a Pathogenic *OPA1* Mutation Exhibit Increased ROS Levels and Downregulation of *FOXG1*

Heterozygous mutations in OPA1 are a common cause of ADOA (Delettre et al., 2000; Alexander et al., 2000). To ensure that the changes detected in our genetically engineered hESCs were not caused by

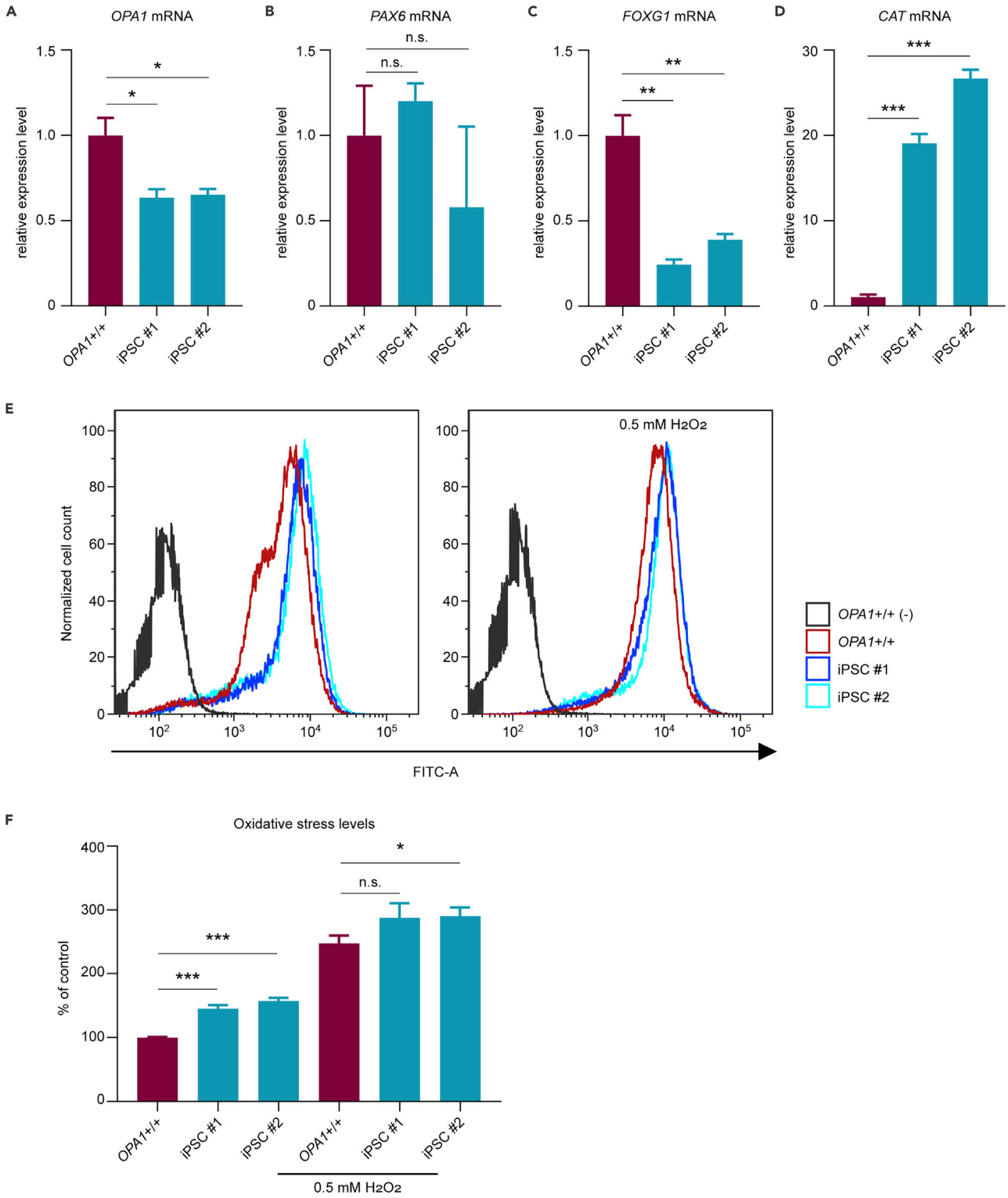

Figure 7. Patient-Derived iPSCs Harboring a Pathogenic *OPA1* Mutation Exhibit Increased ROS Levels and Downregulation of *FOXG1*

(A–D) (A) *OPA1* mRNA, (B) *PAX6*, (C) *FOXG1*, and (D) *CAT* mRNA expression levels in day 11 NPCs differentiated from iPSC lines derived from two donors diagnosed with ADOA.

(E) Representative flow cytometry analysis of *OPA1*+/+ hESCs, iPSC #1, and iPSC #2 labeled with the oxidative stress indicator CM-H2DCFDA. Unlabeled hESCs (–) were used as negative control. hESCs and iPSCs that were incubated with 0.5 mM H_2O_2 were used as positive control.

Figure 7. *Continued*

(F) Quantification of flow cytometry measurements in iPSC #1 and iPSC #2. Arithmetic mean values were normalized to the values of labeled *OPA1+/+* hESCs. Mean ± SEM, N = 3 independent experiments and N = 2 technical replicates. Student's t test was used to analyze difference between two groups. n.s. not significant. *p < 0.05, **p < 0.01, ***p < 0.001.

off-target effects by CRISPR-Cas9, we generated induced pluripotent stem cells (iPSCs) derived from two male donors who carry the inactivating *OPA1* c.2873_2876delTTAG mutation. First, we assessed *OPA1* mRNA expression and found that mRNA expression levels were reduced by 35%–40% compared with *OPA1+/+* NPCs (Figure 7A). Next, we found that *PAX6* mRNA expression levels were similar between patient iPSC- and hESC-derived NPCs (Figure 7B). Moreover, *FOXG1* (Figure 7C) and *CAT* (Figure 7D) mRNA expression levels were down- and upregulated in patient iPSC-derived NPCs, respectively. Next, we used the ROS indicator CM-H2DCFDA and further demonstrated that ROS levels were markedly increased in patient-derived iPSCs (Figures 7E and 7F). Taken together, these results indicate that *OPA1* haploinsufficiency is accompanied by aberrant nuclear DNA methylation and changed transcriptional circuitry.

DISCUSSION

Our study shows for the first time that *OPA1* haploinsufficiency correlates with aberrant nuclear DNA methylation patterns as well as a significantly altered transcriptional circuitry and differentiation potential of NPCs (Figure 8).

The role of OPA1 during physiologic and pathologic neural development remains incompletely understood. We observed a severe loss of DLX1/DLX2-positive neurons when OPA1 protein levels were reduced by 50%. Studies using mouse models have previously shown that Dlx1 and Dlx2 are expressed in the developing retinal neuroepithelium (Eisenstat et al., 1999) and are needed for the terminal differentiation of late-born RGCs (de Melo et al., 2005). Moreover, *Dlx1/Dlx2* double-null mice exhibit up to 30% reduced numbers of RGCs, whereas formation of other retinal neuronal cell types is not affected. In addition to Dlx1/2, loss of *Sfrp1* expression (Esteve et al., 2003) and forced expression of NeuroD factors (Cherry et al., 2011) are known to dysregulate retinal cell diversity in mice and chicken. Strikingly, we find impaired expression of DLX1/2 and SFRP1 as well as an upregulation of NEUROD4 when OPA1 levels are reduced, which may explain the loss of RGCs observed in patients with ADOA.

Our transcriptome analysis in NPCs substantiates the relevance of balanced OPA1 levels for proper neural cell homeostasis. One TF that we find consistently repressed in our study is the pioneer factor *FOXG1*, which is predominantly expressed in the developing neuroepithelium, retina, and optic chiasm. A previous study found that FOXG1 is crucial for GABAergic neuronal formation and retinal development because *Foxg1−/−* mice exhibit eye abnormalities (Xuan et al., 1995). Importantly, *Foxg1−/−* telencephalic progenitors fail to generate Dlx1-and Dlx2-positive neurons (Xuan et al., 1995). Other evidence that links FOXG1 to the generation of DLX1/2+ neurons stems from a recent report demonstrating that *FOXG1* upregulation is responsible for the overproduction of GABAergic neurons in brain organoids derived from iPSCs obtained from patients with autism spectrum disorder (Mariani et al., 2015). In addition, studies in mice and chicken showed that loss of *Foxg1* expression results in RGC axonal misprojection and pathfinding defects (Yuasa et al., 1996; Pratt et al., 2004). Our gene expression analyses in hESC-derived NPCs and neurons also suggest that FOXG1 is a direct regulator of human GABAergic neuronal formation and retinal development.

Recently, iPSCs derived from patients carrying heterozygous mutations in *OPA1* and having an inherited form of Parkinson disease (PD) were generated and used to investigate dopaminergic neuronal development. The authors found fragmented mitochondria, a decrease in respiration, and a decrease in neuronal viability, as well as an increase in ROS (Iannielli et al., 2018). Although we also observe an increase in ROS and sensitivity to apoptotic stimuli, we only find subtle changes in mitochondrial morphology including increased intercristae distance, reduced circumference, and a trend to more fragmented mitochondria in *OPA1+/−* hESCs. Overall, the phenotype in PD patient-derived iPSCs seems more severe than the one observed in *OPA1* haploinsufficient hESCs and ADOA patient-derived iPSCs. It is possible that this is because PD is a more complex disease with potential additional epigenetic and genetic changes in contrast to familial optic atrophy with a single-gene mutation. Other studies also show significant mitochondrial fragmentation in mouse cerebellar granule (Jahani-Asl et al., 2011) and HeLa cells (Arnoult et al., 2005). In these studies OPA1 expression was almost completely abolished, whereas in our cells 50% OPA1 proteins remain, which might explain the mild changes in mitochondrial morphology in our

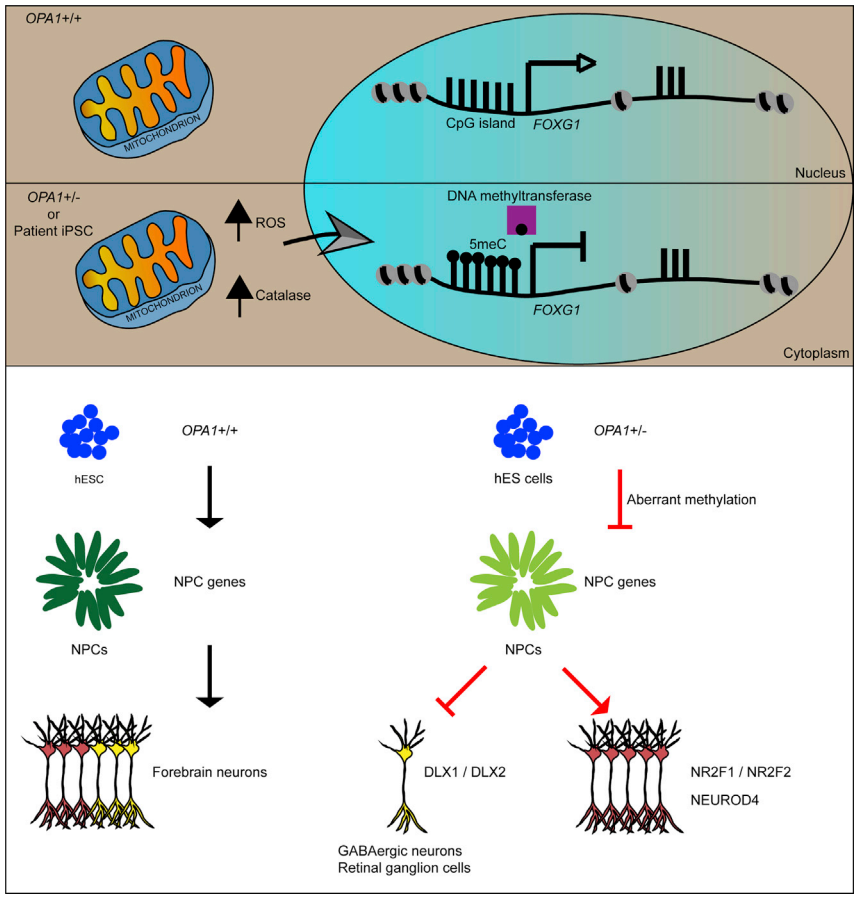

Figure 8. Schematics Illustrating the Metabolic and Epigenetic Changes in *OPA1* Haploinsufficient Cells, Which May Contribute to Altered Neuronal Differentiation

cells. In line with this, a recent study using *OPA1* haploinsufficient iPSCs derived from patients with syndromic parkinsonism also shows only subtle changes in the mitochondrial ultrastructure in iPSC-derived dopaminergic neurons (Jonikas et al., 2018).

A fascinating question is how *OPA1* haploinsufficiency impacts on nuclear DNA methylation at specific sites, such as the *FOXG1* and *ATP10D* promoters. Epigenetic pathways and transcriptional regulation are influenced by non-protein-coding RNA molecules. For instance, the murine long non-coding RNA Kcnq1ot1 recruits the DNA methyltransferase Dnmt1 to CpG islands of imprinted genes (Mohammad et al., 2010), and the natural antisense transcript AS1DHRS4 controls localization of DNMTs to the promoter regions of transcripts DHRS4L1 and DHRS4L2 (Li et al., 2012). Given that the DNA methylation changes we observe in *OPA1+/–* NPCs are loci specific, it is possible that expression and availability of non-coding RNAs that regulate DNA methylation is affected in *OPA1+/–* NPCs.

Enzymes catalyzing epigenetic changes require specific metabolites as sources of acetyl or methyl groups (Katada et al., 2012; Lu and Thompson, 2012). Small metabolites such as SAM, SAH, and alpha-ketoglutarate establish a link between mitochondrial metabolism and epigenetics (Matilainen et al., 2017). We find similar SAM/SAH and succinate/alpha-ketoglutarate levels in *OPA1+/–* and *OPA1+/+* cells, suggesting that the observed changes in DNA methylation are not caused by alterations of these small metabolites. Previously, it has been shown that oxidative stress causes aberrant DNA methylation and transcriptional silencing (O'Hagan et al., 2011). The authors reveal that DNMT1 is targeted to damaged chromatin, forming a complex with DNMT3B and polycomb repressive complex 4 (O'Hagan et al., 2011), and show that hydrogen peroxide treatment causes a relocalization of these proteins to promoter CpG islands. Importantly, we find that *OPA1* haploinsufficiency results in increased oxidative stress and ROS accumulation

in *OPA1*+/− hESCs and ADOA patient-derived iPSCs. It is well possible that altered ROS levels play a role in the DNA methylation changes we described. Supporting this notion, mitochondrial dysfunction and increased ROS levels have recently been described to cause specific promoter hypermethylation and decreased expression of microRNA-663 in cancer cell lines (Carden et al., 2017). Exogenous and endogenous ROS are also known to affect neural stem cell renewal and proliferation. For instance, Le Belle et al. show that brain-derived neural progenitors maintain a high ROS status and are responsive to ROS stimulation leading to posttranslational oxidative inactivation of PTEN, and activation of PI3K/Akt signaling pathway, which is required for NPC self-renewal (Le Belle et al., 2011). Another study by Chui et al. demonstrated that selective removal of histone-lysine N-methyltransferase *PRDM16* in NPCs leads to abnormal neuronal composition and organization in the mouse brain by inducing excessive ROS (Chui et al., 2020). Our results together with these studies suggest that activation of specific pathways by ROS signaling is context dependent and may influence various pathways during cell fate specification.

In conclusion, we provide evidence that *OPA1* haploinsufficient cells exhibit increased oxidative stress, aberrant nuclear DNA methylation, and a significantly altered transcriptional circuitry.

Limitations of the Study

Although we addressed DNA methylation changes in the promoter regions of selected down-regulated genes, we did not explore this for up-regulated genes or in a global context. Moreover, we did not assess cell death under stress conditions in iPSC-derived neurons, and performed the mitochondrial respiration assay in two not three independent experiments, although each with 10–40 replicates. In addition, although we observed an increase in ROS that might contribute to the aberrant DNA methylation, we were not able to identify the exact mechanism by which *OPA1* haploinsufficiency contributes to these changes in nuclear DNA methylation. Defining primary versus secondary changes related to OPA1 will be exciting to explore in the future.

Resource Availability

Lead Contact

Further information and requests for resources and reagents should be directed to and will be fulfilled by the Lead Contact, Judith Staerk (judith.staerk@ncmm.uio.no).

Materials Availability

There may be restrictions or delays to the availability of hESC and iPSC lines due to our need to maintain the stock and patient consent. Availability of iPSC lines will require a Materials Transfer Agreement.

Data and Code Availability

Access to data that support the findings of this study are available from the authors on reasonable request. RNA-seq information including all raw data has been deposited at Gene Expression Omnibus under GSE117976: https://www.ncbi.nlm.nih.gov/geo/query/acc.cgi?acc=GSE117976.

METHODS

All methods can be found in the accompanying Transparent Methods supplemental file.

SUPPLEMENTAL INFORMATION

Supplemental Information can be found online at https://doi.org/10.1016/j.isci.2020.101154.

ACKNOWLEDGMENTS

This work was supported by the Research Council of Norway, The Regional Health Authority for South-Eastern Norway, Novo Nordisk Foundation, Denmark, the University of Oslo, Norway and the European Union Seventh Framework Programme (FP7-PEOPLE-2013-COFUND) under grant agreement n° 609020 - Scientia Fellows. We thank the patients for agreeing to participate in this study. We thank Marianne Smestad and Ulrikke Brinch Dahl at the core facility for Advanced EM at OUS, which is funded by the South East Regional Health Authority, Norway, for technical assistance. The HPLC-MS/MS analyses of DNA modifications were performed by the Proteomics and Modomics Experimental Core Facility (PROMEC), Norwegian University of Science and Technology (NTNU), Trondheim, Norway. PROMEC is funded by the Faculty of

Medicine and Health Sciences at NTNU and the Central Norway Regional Health Authority, Norway. We thank the Medical Bioinformatics Centre of Turku Centre for Biotechnology for the copy number data analysis. The Centre is supported by the University of Turku, Åbo Akademi University, and Biocenter Finland, Finland.

AUTHOR CONTRIBUTIONS

S.C. and J.S. designed the study. J.S. generated genetically modified hESC and patient iPSC lines. S.C., A.C.-P., V.J., C.P., S.B., B.T., D.T.C., M.R., A. Brech, and S.H.B. performed experiments, A.H. performed bioinformatics analysis. A. Boschi provided primary patient material. S.C., A.H., V.J., A. Brech, S.H.B., E.A.N., L.H., K.T., and J.S. interpreted results. S.C. and J.S. wrote the manuscript. All authors commented and approved the final version.

DECLARATION OF INTERESTS

The authors declare no competing interests.

Received: October 29, 2019
Revised: April 3, 2020
Accepted: May 6, 2020
Published: June 26, 2020

REFERENCES

Akepati, V.R., Muller, E.C., Otto, A., Strauss, H.M., Portwich, M., and Alexander, C. (2008). Characterization of OPA1 isoforms isolated from mouse tissues. J. Neurochem. *106*, 372–383.

Alavi, M.V., Bette, S., Schimpf, S., Schuettauf, F., Schraermeyer, U., Wehrl, H.F., Ruttiger, L., Beck, S.C., Tonagel, F., Pichler, B.J., et al. (2007). A splice site mutation in the murine Opa1 gene features pathology of autosomal dominant optic atrophy. Brain *130*, 1029–1042.

Alexander, C., Votruba, M., Pesch, U.E., Thiselton, D.L., Mayer, S., Moore, A., Rodriguez, M., Kellner, U., Leo-Kottler, B., Auburger, G., et al. (2000). OPA1, encoding a dynamin-related GTPase, is mutated in autosomal dominant optic atrophy linked to chromosome 3q28. Nat. Genet. *26*, 211–215.

Anderson, S.A., Eisenstat, D.D., Shi, L., and Rubenstein, J.L. (1997). Interneuron migration from basal forebrain to neocortex: dependence on Dlx genes. Science *278*, 474–476.

Arnoult, D., Grodet, A., Lee, Y.J., Estaquier, J., and Blackstone, C. (2005). Release of OPA1 during apoptosis participates in the rapid and complete release of cytochrome c and subsequent mitochondrial fragmentation. J. Biol. Chem. *280*, 35742–35750.

Beaubien, F., and Cloutier, J.-F. (2009). Differential expression of slitrk family members in the mouse nervous system. Dev. Dyn. *238*, 3285–3296.

Carden, T., Singh, B., Mooga, V., Bajpai, P., and Singh, K.K. (2017). Epigenetic modification of miR-663 controls mitochondria-to-nucleus retrograde signaling and tumor progression. J. Biol. Chem. *292*, 20694–20706.

Chambers, S.M., Fasano, C.A., Papapetrou, E.P., Tomishima, M., Sadelain, M., and Studer, L. (2009). Highly efficient neural conversion of human ES and iPS cells by dual inhibition of SMAD signaling. Nat. Biotechnol. *27*, 275–280.

Chan, D.C. (2012). Fusion and fission: interlinked processes critical for mitochondrial health. Annu. Rev. Genet. *46*, 265–287.

Cherry, T.J., Wang, S., Bormuth, I., Schwab, M., Olson, J., and Cepko, C.L. (2011). NeuroD factors regulate cell fate and neurite stratification in the developing retina. J. Neurosci. *31*, 7365–7379.

Chui, A., Zhang, Q., Dai, Q., and Shi, S.H. (2020). Oxidative stress regulates progenitor behavior and cortical neurogenesis. Development *147*, dev184150.

Davies, V.J., Hollins, A.J., Piechota, M.J., Yip, W., Davies, J.R., White, K.E., Nicols, P.P., Boulton, M.E., and Votruba, M. (2007). Opa1 deficiency in a mouse model of autosomal dominant optic atrophy impairs mitochondrial morphology, optic nerve structure and visual function. Hum. Mol. Genet. *16*, 1307–1318.

de Melo, J., Du, G., Fonseca, M., Gillespie, L.-A., Turk, W.J., Rubenstein, J.L.R., and Eisenstat, D.D. (2005). Dlx1 and Dlx2 function is necessary for terminal differentiation and survival of late-born retinal ganglion cells in the developing mouse retina. Development *132*, 311–322.

Deglincerti, A., Etoc, F., Ozair, M.Z., and Brivanlou, A.H. (2016). Chapter six - self-organization of spatial patterning in human embryonic stem cells. In Current Topics in Developmental Biology, *116*, P.M. Wassarman, ed (Academic Press), pp. 99–113.

Del Dotto, V., Mishra, P., Vidoni, S., Fogazza, M., Maresca, A., Caporali, L., McCaffery, J.M., Cappelletti, M., Baruffini, E., Lenaers, G., et al. (2017). OPA1 isoforms in the hierarchical organization of mitochondrial functions. Cell Rep. *19*, 2557–2571.

Delettre, C., Griffoin, J.M., Kaplan, J., Dollfus, H., Lorenz, B., Faivre, L., Lenaers, G., Belenguer, P., and Hamel, C.P. (2001). Mutation spectrum and splicing variants in the OPA1 gene. Hum. Genet. *109*, 584–591.

Delettre, C., Lenaers, G., Griffoin, J.M., Gigarel, N., Lorenzo, C., Belenguer, P., Pelloquin, L., Grosgeorge, J., Turc-Carel, C., Perret, E., et al. (2000). Nuclear gene OPA1, encoding a mitochondrial dynamin-related protein, is mutated in dominant optic atrophy. Nat. Genet. *26*, 207–210.

Eisenstat, D.D., Liu, J.K., Mione, M., Zhong, W., Yu, G., Anderson, S.A., Ghattas, I., Puelles, L., and Rubenstein, J.L.R. (1999). DLX-1, DLX-2, and DLX-5 expression define distinct stages of basal forebrain differentiation. J. Comp. Neurol. *414*, 217–237.

Esteve, P., Trousse, F., Rodríguez, J., and Bovolenta, P. (2003). SFRP1 modulates retina cell differentiation through aβ -catenin-independent mechanism. J. Cell Sci. *116*, 2471–2481.

Herrera, F.J., Yamaguchi, T., Roelink, H., and Tjian, R. (2014). Core promoter factor TAF9B regulates neuronal gene expression. Elife *3*, e02559.

Hevner, R.F., Shi, L., Justice, N., Hsueh, Y., Sheng, M., Smiga, S., Bulfone, A., Goffinet, A.M., Campagnoni, A.T., and Rubenstein, J.L. (2001). Tbr1 regulates differentiation of the preplate and layer 6. Neuron *29*, 353–366.

Ho, T.T., Warr, M.R., Adelman, E.R., Lansinger, O.M., Flach, J., Verovskaya, E.V., Figueroa, M.E., and Passegue, E. (2017). Autophagy maintains the metabolism and function of young and old stem cells. Nature *543*, 205–210.

Iannielli, A., Bido, S., Folladori, L., Segnali, A., Cancellieri, C., Maresca, A., Massimino, L., Rubio, A., Morabito, G., Caporali, L., et al. (2018). Pharmacological inhibition of necroptosis

protects from dopaminergic neuronal cell death in Parkinson's disease models. Cell Rep. *22*, 2066–2079.

Jahani-Asl, A., Pilon-Larose, K., Xu, W., Maclaurin, J.G., Park, D.S., Mcbride, H.M., and Slack, R.S. (2011). The mitochondrial inner membrane GTPase, optic atrophy 1 (Opa1), restores mitochondrial morphology and promotes neuronal survival following excitotoxicity. J. Biol. Chem. *286*, 4772–4782.

Jonikas, M., Madill, M., Mathy, A., Zekoll, T., Zois, C.E., Wigfield, S., Kurzawa-Akanbi, M., Browne, C., Sims, D., Chinnery, P.F., et al. (2018). Stem cell modeling of mitochondrial parkinsonism reveals key functions of OPA1. Ann. Neurol. *83*, 915–925.

Katada, S., Imhof, A., and Sassone-Corsi, P. (2012). Connecting threads: epigenetics and metabolism. Cell *148*, 24–28.

Le Belle, J.E., Orozco, N.M., Paucar, A.A., Saxe, J.P., Mottahedeh, J., Pyle, A.D., Wu, H., and Kornblum, H.I. (2011). Proliferative neural stem cells have high endogenous ROS levels that regulate self-renewal and neurogenesis in a PI3K/Akt-dependant manner. Cell Stem Cell *8*, 59–71.

Letinic, K., Zoncu, R., and Rakic, P. (2002). Origin of GABAergic neurons in the human neocortex. Nature *417*, 645–649.

Li, Q., Su, Z., Xu, X., Liu, G., Song, X., Wang, R., Sui, X., Liu, T., Chang, X., and Huang, D. (2012). AS1DHRS4, a head-to-head natural antisense transcript, silences the DHRS4 gene cluster in cis and trans. Proc. Natl. Acad. Sci. U S A *109*, 14110–14115.

Lu, C., and Thompson, C.B. (2012). Metabolic regulation of epigenetics. Cell Metab. *16*, 9–17.

MacVicar, T., and Langer, T. (2016). OPA1 processing in cell death and disease - the long and short of it. J. Cell Sci. *129*, 2297–2306.

Mariani, J., Coppola, G., Zhang, P., Abyzov, A., Provini, L., Tomasini, L., Amenduni, M., Szekely, A., Palejev, D., Wilson, M., et al. (2015). FOXG1-Dependent dysregulation of GABA/glutamate neuron differentiation in autism spectrum disorders. Cell *162*, 375–390.

Matilainen, O., Quiros, P.M., and Auwerx, J. (2017). Mitochondria and epigenetics - crosstalk in homeostasis and stress. Trends Cell Biol. *27*, 453–463.

Mirzayans, F., Walter, M.A., Berry, F.B., Link, B.A., Skarie, J.M., Hudson, T.J., Fortin, Y., and Raymond, V. (2007). FOXC1 is required for cell viability and resistance to oxidative stress in the eye through the transcriptional regulation of FOXO1A. Hum. Mol. Genet. *17*, 490–505.

Mohammad, F., Mondal, T., Guseva, N., Pandey, G.K., and Kanduri, C. (2010). Kcnq1ot1 noncoding RNA mediates transcriptional gene silencing by interacting with Dnmt1. Development *137*, 2493–2499.

Nasca, A., Rizza, T., Doimo, M., Legati, A., Ciolfi, A., Diodato, D., Calderan, C., Carrara, G., Lamantea, E., Aiello, C., et al. (2017). Not only dominant, not only optic atrophy: expanding the clinical spectrum associated with OPA1 mutations. Orphanet J. Rare Dis. *12*, 89.

O'Hagan, Heather, M., Wang, W., Sen, S., Destefano Shields, C., Lee, S.S., Zhang, Y.W., Clements, E.G., Cai, Y., van Neste, L., et al. (2011). Oxidative damage targets complexes containing DNA methyltransferases, SIRT1, and polycomb members to promoter CpG islands. Cancer Cell *20*, 606–619.

Pratt, T., Tian, N.M.M.-L., Simpson, T.I., Mason, J.O., and Price, D.J. (2004). The winged helix transcription factor Foxg1 facilitates retinal ganglion cell axon crossing of the ventral midline in the mouse. Development *131*, 3773–3784.

Shi, Y., Kirwan, P., and Livesey, F.J. (2012). Directed differentiation of human pluripotent stem cells to cerebral cortex neurons and neural networks. Nat. Protoc. *7*, 1836–1846.

Spiegel, R., Saada, A., Flannery, P.J., Burte, F., Soiferman, D., Khayat, M., Eisner, V., Vladovski, E., Taylor, R.W., Bindoff, L.A., et al. (2016). Fatal infantile mitochondrial encephalomyopathy, hypertrophic cardiomyopathy and optic atrophy associated with a homozygous OPA1 mutation. J. Med. Genet. *53*, 127–131.

Xuan, S.H., Baptista, C.A., Balas, G., Tao, W.F., Soares, V.C., and Lai, E. (1995). Winged helix transcription factor Bf-1 is essential for the development of the cerebral hemispheres. Neuron *14*, 1141–1152.

Yuasa, J., Hirano, S., Yamagata, M., and Noda, M. (1996). Visual projection map specified by topographic expression of transcription factors in the retina. Nature *382*, 632–635.

iScience, Volume *23*

Supplemental Information

Optic Atrophy 1 Controls Human Neuronal Development by Preventing Aberrant Nuclear DNA Methylation

Safak Caglayan, Adnan Hashim, Artur Cieslar-Pobuda, Vidar Jensen, Sidney Behringer, Burcu Talug, Dinh Toi Chu, Christian Pecquet, Marie Rogne, Andreas Brech, Sverre Henning Brorson, Erlend Arnulf Nagelhus, Luciana Hannibal, Antonella Boschi, Kjetil Taskén, and Judith Staerk

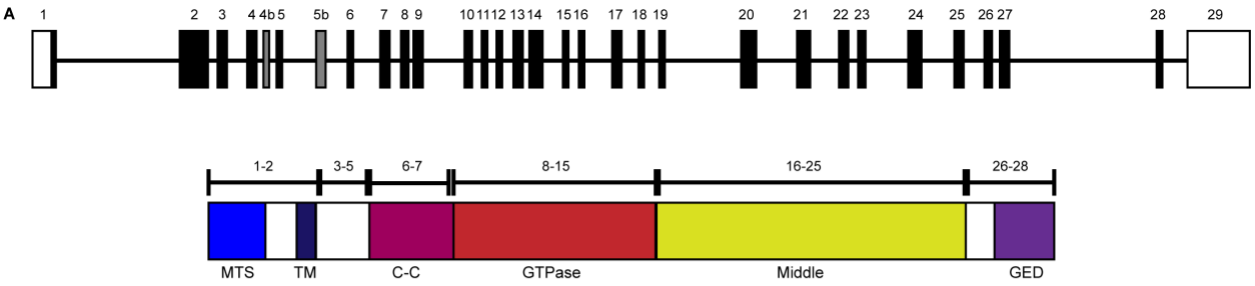
A
1
2
3
4 4b 5
5b
6
7
8 9
10 11 12 13 14
15 16
17
18 19
20
21
22 23
24
25
26 27
28
29
1-2
3-5
6-7
8-15
16-25
26-28
MTS
TM
C-C
GTPase
Middle
GED

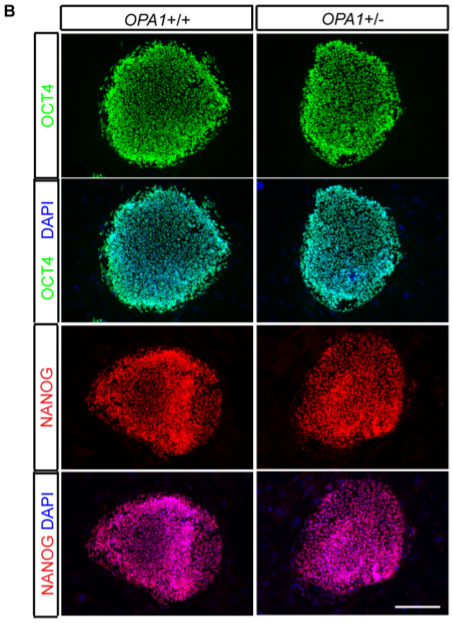
B
OPA1+/+
OPA1+/-
OCT4
OCT4 DAPI
NANOG
NANOG DAPI

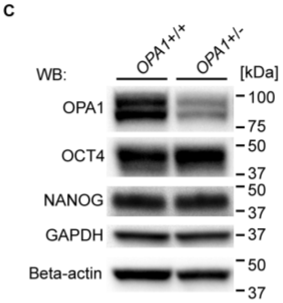
C
WB:
OPA1+/+
OPA1+/-
[kDa]
OPA1
OCT4
NANOG
GAPDH
Beta-actin
100
75
50
37
50
37
37
50
37

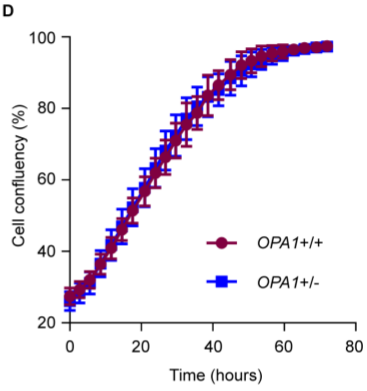
D
Cell confluency (%)
Time (hours)
OPA1+/+
OPA1+/-

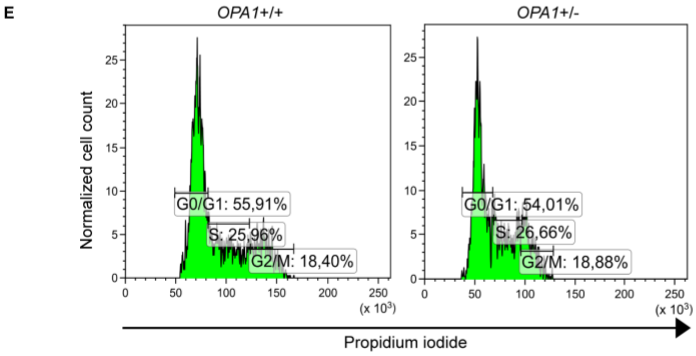
E
OPA1+/+
OPA1+/-
Normalized cell count
G0/G1: 55,91%
S: 25,96%
G2/M: 18,40%
G0/G1: 54,01%
S: 26,66%
G2/M: 18,88%
(x 10³)
Propidium iodide

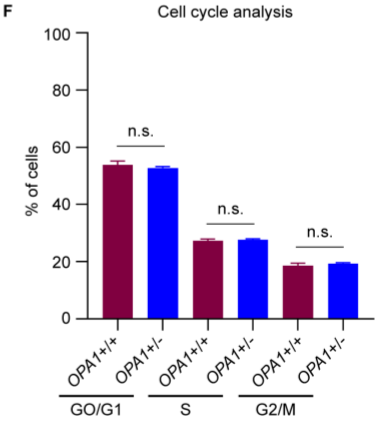
F
Cell cycle analysis
% of cells
n.s.
n.s.
n.s.
OPA1+/+
OPA1+/-
GO/G1
S
G2/M

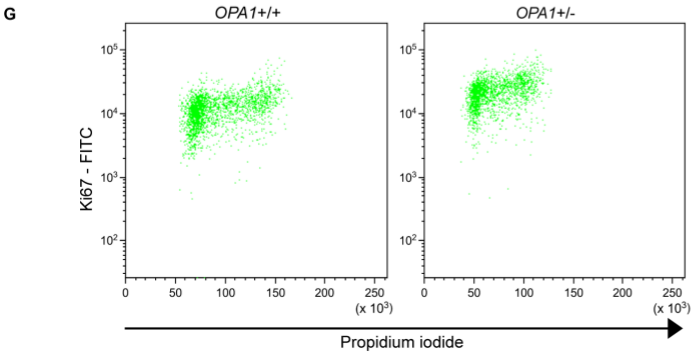
G
OPA1+/+
OPA1+/-
Ki67 - FITC
(x 10³)
Propidium iodide

Figure S1. Schematic representation of OPA1 and characterization of *OPA1*+/- hESCs. Related to Figure 1. A) Genomic and protein domain organization of OPA1. Exon 4b and 5b are alternatively spliced exons in *OPA1* isoform 1. Numbers above protein domains denote exons coding for the respective domains. MTS: mitochondria transport sequence; TM: transmembrane domain; C-C: coiled-coiled domain; GED: GTPase effector domain. Protein domains identified based on (Delettre et al., 2000) and RNA isoforms are depicted according to (Delettre et al., 2001, Akepati et al., 2008). **B)** Immunostainings of *OPA1*+/+ and *OPA1*+/- hESCs using OCT4 and NANOG antibodies. DAPI was used to stain nuclei. Scale bar 200 µm. **C)** Representative immunoblotting images showing OPA1, OCT4, and NANOG protein levels. GAPDH and beta-actin were used as loading controls. **D)** Proliferation rate of hESCs quantified using the Incucyte live cell imaging instrument. **E)** Representative flow cytometry analysis of *OPA1*+/+ and *OPA1*+/- hESCs labeled with fluorescent DNA stain propidium iodide (PI). **F)** Quantification of different cell cycle stages using PI labeling in *OPA1*+/+ and *OPA1*+/- hESCs. Mean ± SEM, N = 4 independent experiments and N = 2 technical replicates. **G)** Representative FACS analysis of *OPA1*+/+ and *OPA1*+/- hESCs labeled with proliferation indicator Ki67 antibody and PI. Similar results were obtained in N ≥ 3 independent experiments. Student's t test was used to analyze difference between two groups. n.s. not significant.

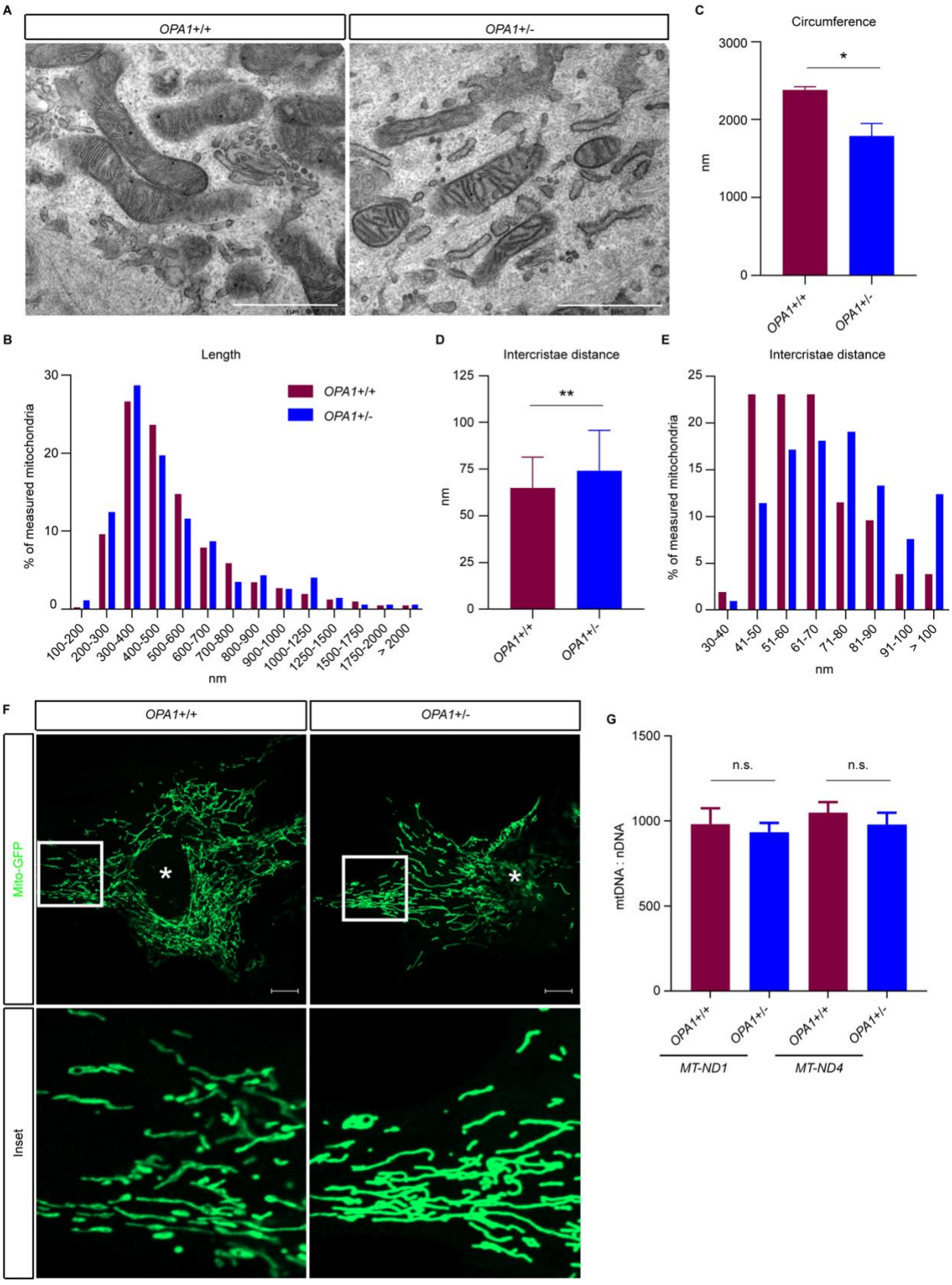
A
OPA1+/+
OPA1+/-
C
Circumference
3000
2000
1000
0
nm
*
OPA1+/+
OPA1+/-
B
Length
30
20
10
0
% of measured mitochondria
OPA1+/+
OPA1+/-
100-200
200-300
300-400
400-500
500-600
600-700
700-800
800-900
900-1000
1000-1250
1250-1500
1500-1750
1750-2000
> 2000
nm
D
Intercristae distance
125
100
75
50
25
0
nm
**
OPA1+/+
OPA1+/-
E
Intercristae distance
25
20
15
10
5
0
% of measured mitochondria
30-40
41-50
51-60
61-70
71-80
81-90
91-100
> 100
nm
F
OPA1+/+
OPA1+/-
Mito-GFP
Inset
G
1500
1000
500
0
mtDNA : nDNA
n.s.
n.s.
OPA1+/+
OPA1+/-
OPA1+/+
OPA1+/-
MT-ND1
MT-ND4

Figure S2. Subtle changes in mitochondrial morphology in *OPA1*+/- hESCs. Related to Figure 1. A) Representative transmission electron microscopy images of *OPA1*+/+ and *OPA1*+/- hESCs. Scale bar 1 µm. **B)** Circumference was reduced in *OPA1*+/- compared to *OPA1*+/+ hESCs. **C)** Mitochondria measurements were binned into categories of length intervals. **D)** Intercristae distances were significantly increased in *OPA1*+/- compared to *OPA1*+/+ hESCs. **E)** Binning of intercristae distances into categories of distance intervals. **F)** Confocal microscopy images of mito-GFP transduced hESCs. * denotes nucleus. Scale bar 10 µm. **G)** Quantification of mitochondrial DNA content relative to nuclear DNA amount by qPCR. Mean ± SEM, N ≥ 3 independent experiments. Student's t test was used to analyze difference between two groups. n.s. not significant, * = $p < 0.05$, ** = $p < 0.01$.

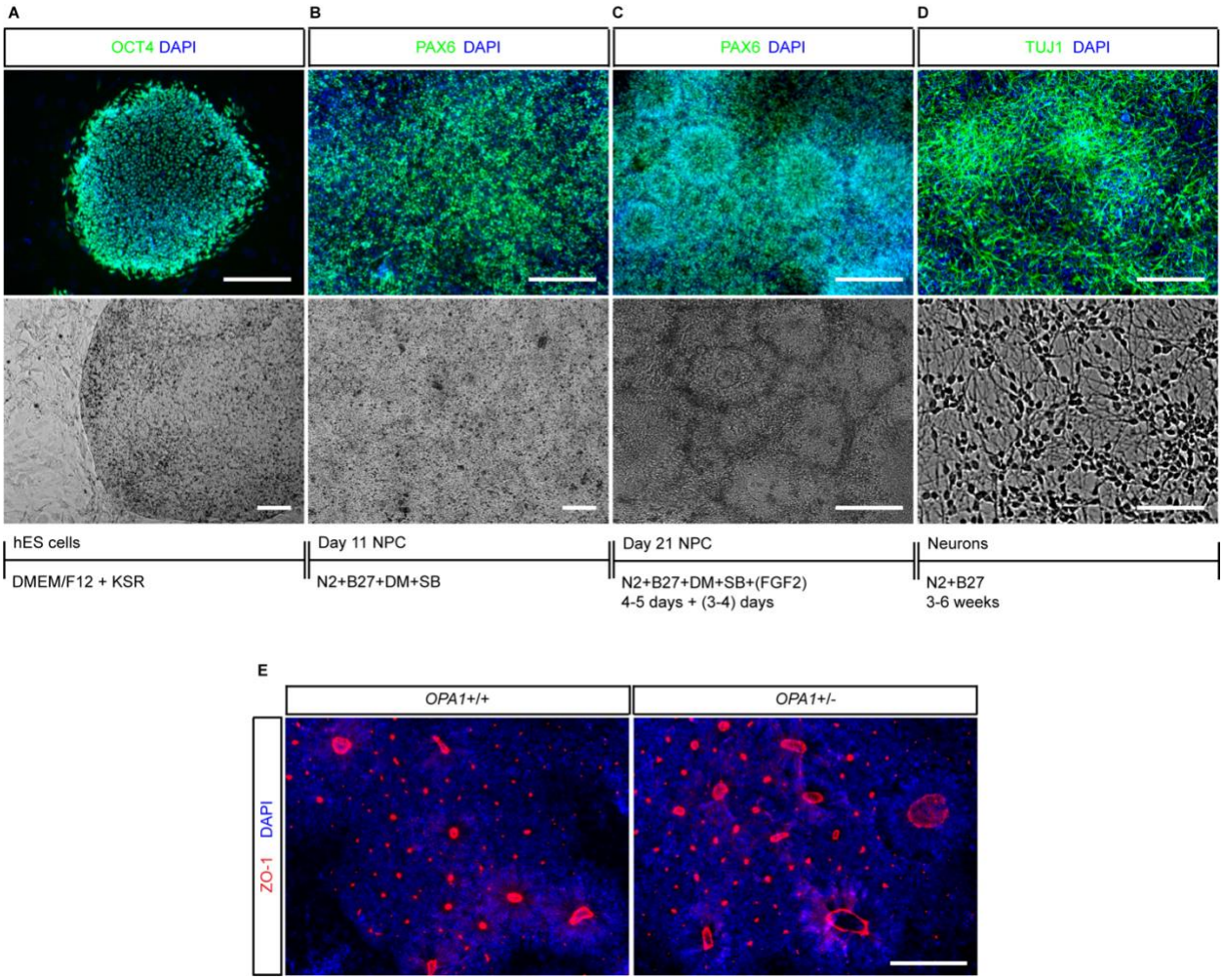

Figure S3. NPC derivation and neuronal differentiation. Related to Figures 2, 3, 4, and 5. A) OCT4 positive hESCs were maintained in DMEM/F12 media containing FGF2. **B)** Neural differentiation was induced with media containing N2/B27 together with dual SMAD inhibitors. Bright-field and immunostaining images of day 11 NPCs. **C)** PAX6-positive NPCs forming rosettes as shown by bright-field and fluorescence microscopy in week 3 NPCs. **D)** Neuronal layers as shown by bright-field and immunostaining images were derived 3-6 weeks after NPC passaging. **E)** Rosette formation by NPCs shown by ZO-1 marker. DAPI was used to stain nuclei. Scale bar 50 µm in panel D and 200 µm in panels A, B, C and E.

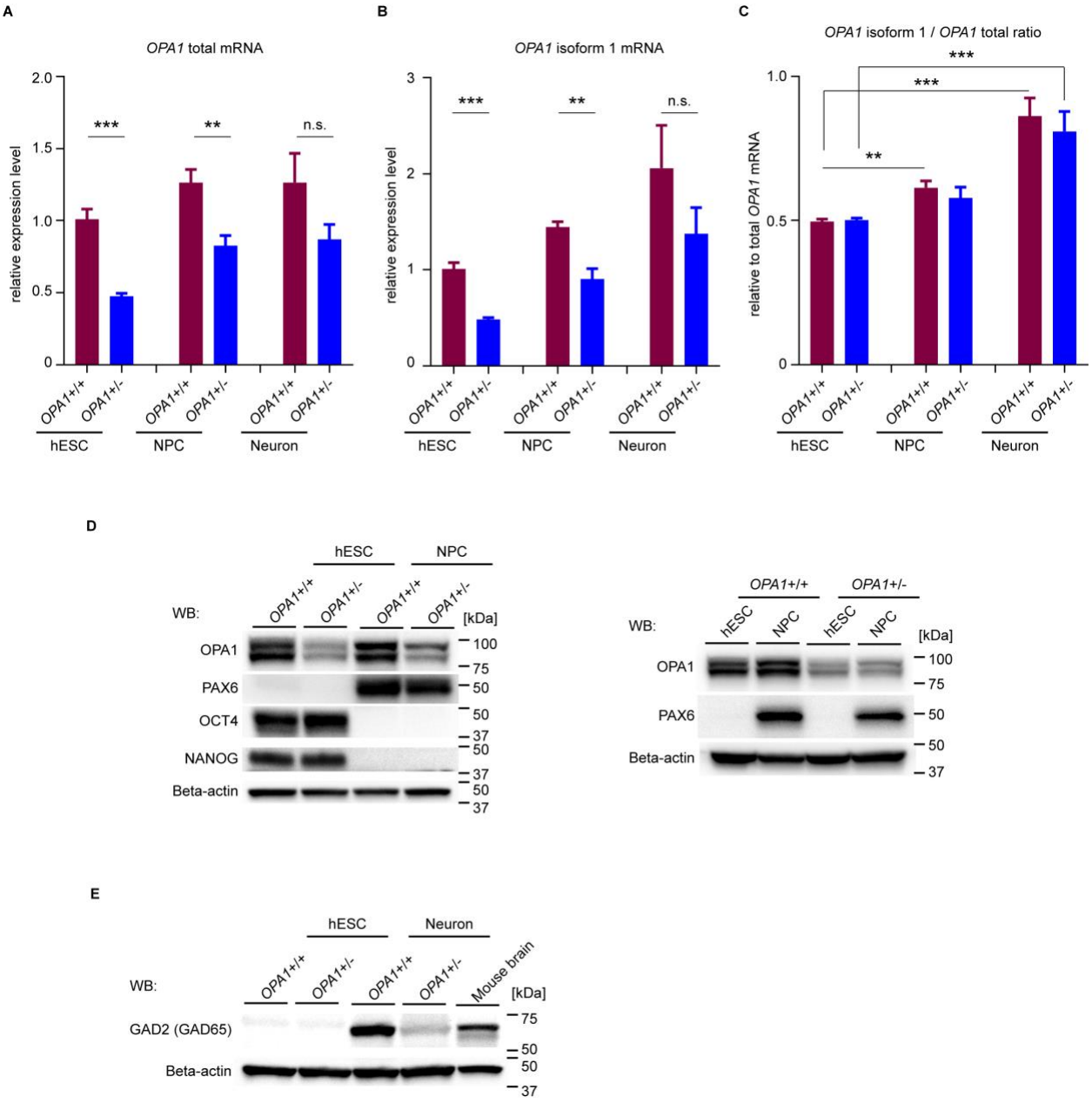

Figure S4. Characterization of *OPA1+/-* and *OPA1+/+* hESCs, NPCs and neurons. Related to Figures 1, 2, 3, and 4. A) QRT-PCR analysis of *OPA1* mRNA expression levels in hESCs, week 3 NPCs and neurons. **B)** *OPA1* isoform 1 transcript levels quantified by qRT-PCR. **C)** Ratio of isoform 1 to total *OPA1* transcript levels. Mean ± SEM, N ≥ 3 independent experiments. **D)** Immunoblotting validating NPC derivation and OPA1 upregulation in NPCs derived from hESCs. OCT4 and NANOG were used as pluripotency marker, PAX6 was used as neural differentiation marker. Beta-actin was used as loading control. **E)** Immunoblotting image of GAD2/GAD65 in *OPA1+/+* and *OPA1+/-* hESCs and neurons. Beta actin was used as loading control. Student's t test was used to analyze difference between two groups. n.s. not significant. ** = $p < 0.01$, *** = $p < 0.001$.

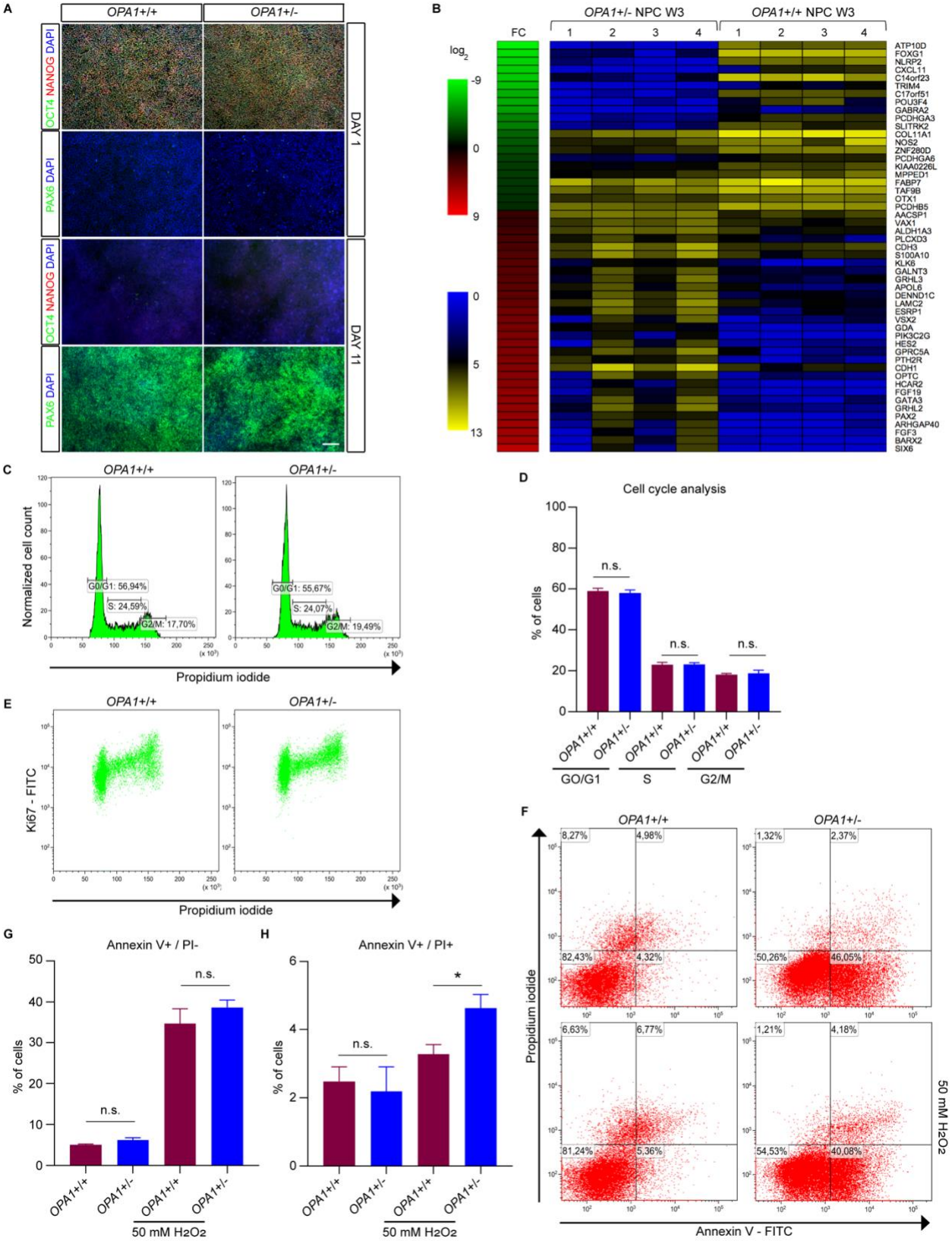
A
OPA1+/+
OPA1+/-
OCT4 NANOG DAPI
PAX6 DAPI
DAY 1
DAY 11
B
OPA1+/- NPC W3
OPA1+/+ NPC W3
FC
log2
ATP10D
FOXG1
NLRP2
CXCL11
C14orf23
TRIM4
C17orf51
POU3F4
GABRA2
PCDHGA3
SLITRK2
COL11A1
NOS2
ZNF280D
PCDHGA6
KIAA0226L
MPPED1
FABP7
TAF9B
OTX1
PCDHB5
AACSP1
VAX1
ALDH1A3
PLCXD3
CDH3
S100A10
KLK6
GALNT3
GRHL3
APOL6
DENND1C
LAMC2
ESRP1
VSX2
GDA
PIK3C2G
HES2
GPRC5A
PTH2R
CDH1
OPTC
HCAR2
FGF19
GATA3
GRHL2
PAX2
ARHGAP40
FGF3
BARX2
SIX6
C
Normalized cell count
G0/G1: 56,94%
S: 24,59%
G2/M: 17,70%
G0/G1: 55,67%
S: 24,07%
G2/M: 19,49%
Propidium iodide
D
Cell cycle analysis
% of cells
n.s.
GO/G1
S
G2/M
E
Ki67 - FITC
Propidium iodide
F
Propidium iodide
Annexin V - FITC
50 mM H2O2
8,27%
4,98%
82,43%
4,32%
1,32%
2,37%
50,26%
46,05%
6,63%
6,77%
81,24%
5,36%
1,21%
4,18%
54,53%
40,08%
G
Annexin V+ / PI-
% of cells
50 mM H2O2
H
Annexin V+ / PI+
*

Figure S5. Transcriptional analysis of *OPA1*+/+ and *OPA1*+/- week 3 NPCs. Related to Figure 5 and Table S3. A) Immunostaining of hESC layers on day 1 before induction of neural differentiation and of NPC layers at day 11 of differentiation. OCT4 and NANOG were used as pluripotency marker, PAX6 was used as neural differentiation marker. Scale bar 200 µm. **B)** Log_2 fold-change and expression heat-maps of selected down- (green) and up- (red) regulated genes in *OPA1*+/- compared to *OPA1*+/+ week 3 NPCs. FC = fold change. Expression intensities are displayed from blue (low expression) to yellow (high expression). **C)** Representative flow cytometry analysis of *OPA1*+/+ and *OPA1*+/- NPCs labeled with fluorescent DNA stain propidium iodide (PI). **D)** Quantification of cell cycle stages using PI labeling in *OPA1*+/+ and *OPA1*+/- NPCs. Mean ± SEM, N = 3 independent experiments and N = 2 technical replicates. **E)** Representative FACS analysis of *OPA1*+/+ and *OPA1*+/- NPCs labeled with the proliferation indicator Ki67 antibody and PI. Similar results were obtained in N = 3 independent experiments. **F)** Representative flow cytometry analysis of *OPA1*+/+ and *OPA1*+/- NPCs labeled with the early-apoptosis indicator Annexin V and late-apoptosis indicator PI. NPCs were incubated with 50 mM H_2O_2 to assess sensitivity to apoptotic stimuli. **G)** Quantification of early-apoptotic Annexin V+ / PI- NPCs. Percentage of labeled cells in total gated cells are shown. **H)** Quantification of late-apoptotic Annexin V+ / PI+ NPCs. Percentage of labeled cells in total gated cells are shown. Mean ± SEM, N ≥ 4 independent experiments and N = 2 technical replicates. Student's t test was used to analyze difference between two groups. n.s. not significant, * = $p < 0.05$.

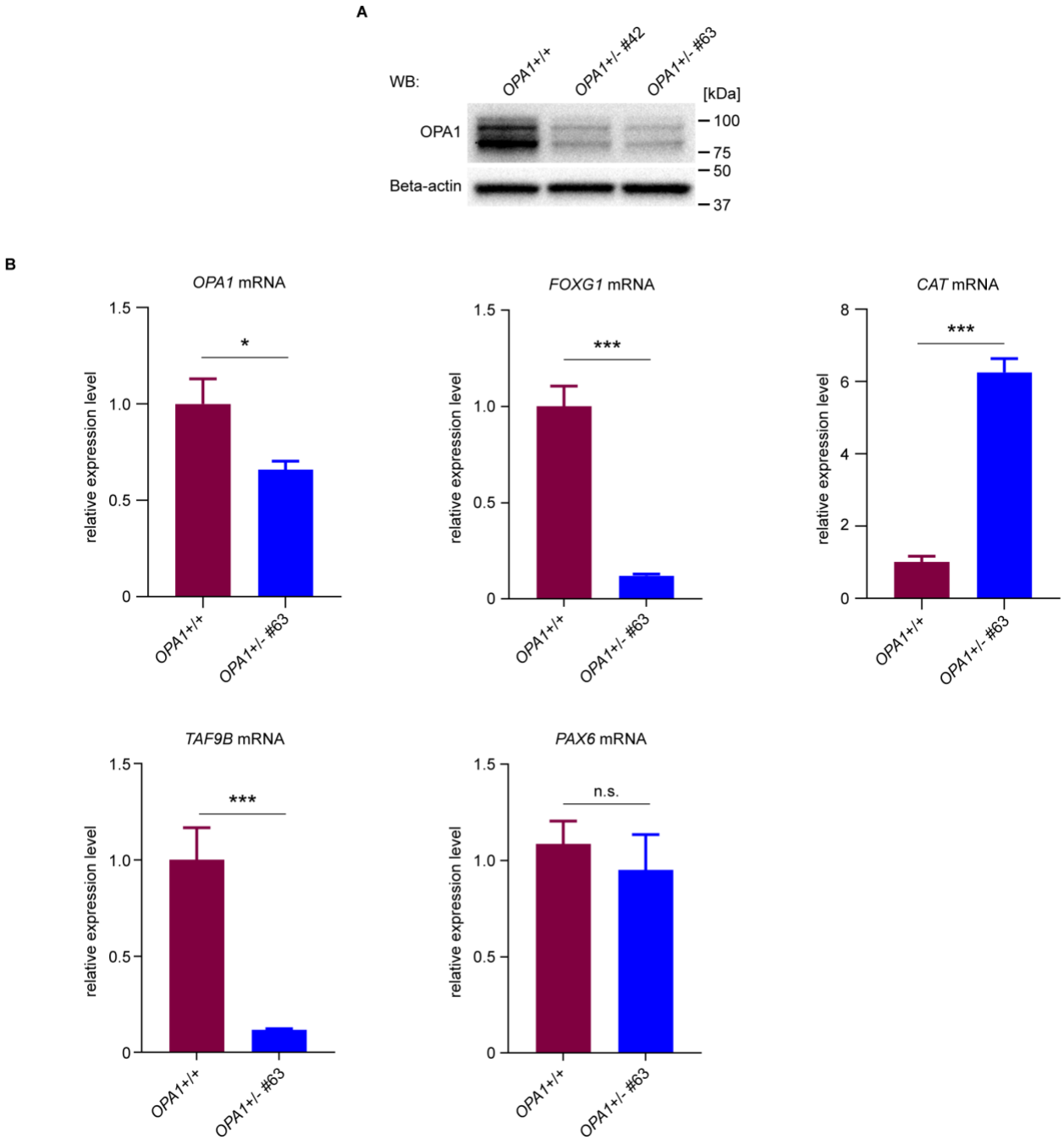

Figure S6. Confirmation of key findings in the second, independently derived *OPA1+/-* hESC line #63. Related to Figures 5 and 6. A) Immunoblotting of OPA1 in *OPA1*+/+ and *OPA1*+/- hESC lines #42 and #63. Beta-actin was used as loading control. **B)** *OPA1*, *PAX6*, *FOXG1*, *TAF9B* and *CAT* mRNA expression levels in NPCs derived from *OPA1*+/+ and *OPA1*+/- #63 hESCs. mRNA levels were normalized to transcript levels in *OPA1*+/+ NPCs. Mean ± SEM, N ≥ 3 independent samples were analyzed for each genotype. Student's t test was used to analyze the differences between two groups. n.s. not significant, * = $p < 0.05$, *** = $p < 0.001$.

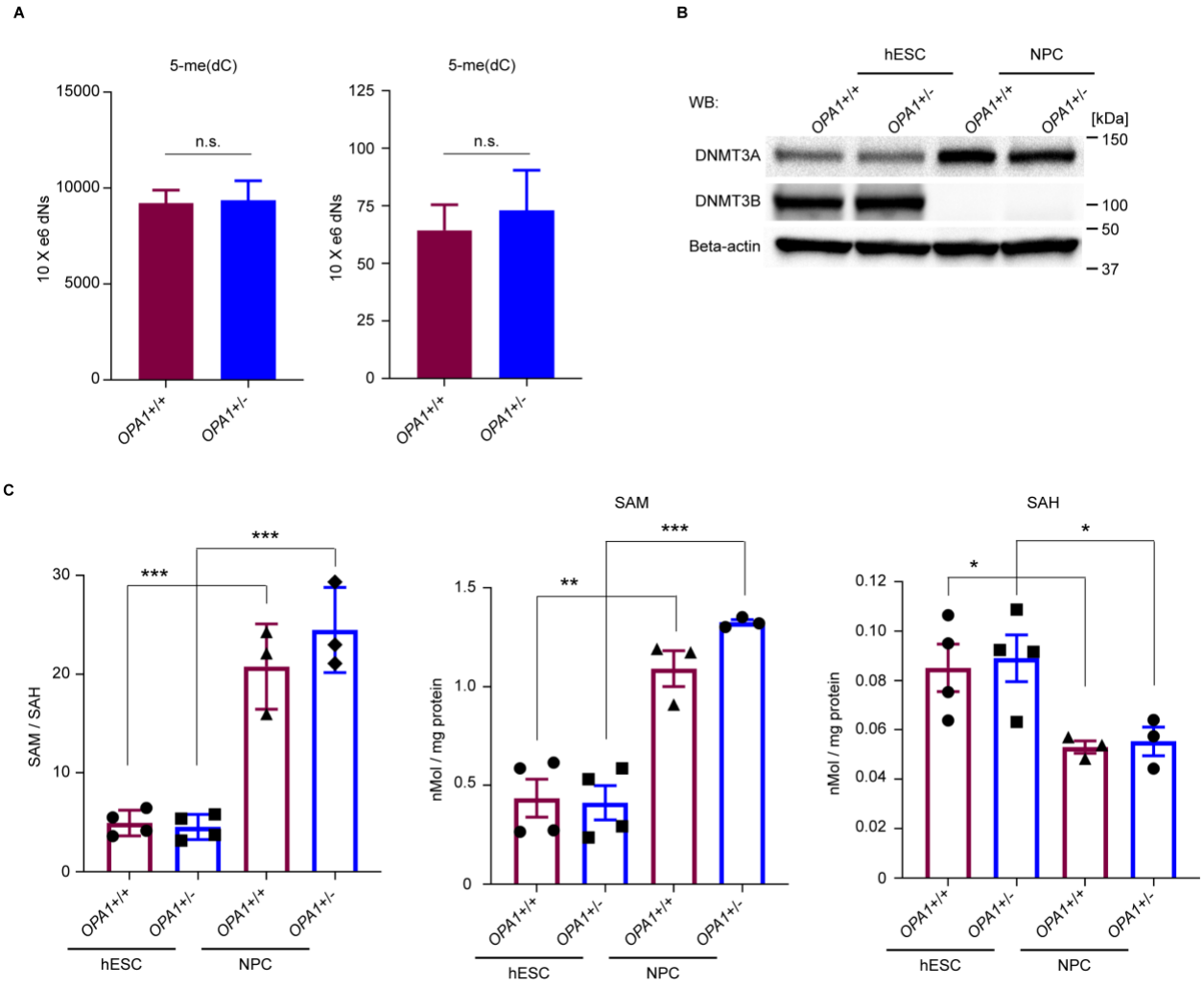

Figure S7. Mass spectrometry and immunoblotting analysis of epigenetic and metabolic changes. Related to Figure 6. A) Total methylation and hydroxymethylation levels were analyzed in *OPA1*+/+ and *OPA1*+/- week 3 NPCs. Quantification of 5-me(dC) and 5-hm(dC) levels as determined by mass spectrometry. Mean ± SEM, N = 3 independent samples were analyzed for each genotype. **B)** Immunoblotting of DNMT3A and DNMT3B in *OPA1*+/+ and *OPA1*+/- hESCs and NPCs. **C)** SAM / SAH ratio in *OPA1*+/+ and *OPA1*+/- hESCs and NPCs measured by mass spectrometry analysis. SAM and SAH levels were quantified in control and *OPA1*+/- hESCs and NPCs. Mean ± SEM, N ≥ 3 independent samples were assessed for each genotype and cell type. Student's t test was used to analyze the differences between two groups. n.s. not significant. * = $p < 0.05$, ** = $p < 0.01$, *** = $p < 0.001$.

Transparent Methods

Table S4. Oligonucleotides used in this study. Related to Figures 1-7, and Figures S4 and S6.

Oligonucleotide name	**Sequence (5' -> 3')**
ATP10D promoter bisulfite FW	TGAGATTGTAAGGGTTTTGGG
ATP10D promoter bisulfite RV	TCACTTAAACATCTCCCAAACTC
ATP10D RT-PCR FW	AAGTGGCAGACATTGGGATAG
ATP10D RT-PCR RV	GAATCATGTTGGAAAGCCGTG
B2M PCR FW	CACTGAAAAAGATGAGTATGCC
B2M PCR RV	AACATTCCCTGACAATCCC
CAT RT-PCR FW	CAGATAGCCTTCGACCCAAG
CAT RT-PCR RV	GTAGGGACAGTTCACAGGTATATG
DLX1 RT-PCR FW	CAGCCCCTACATCAGTTCG
DLX1 RT-PCR RV	TCCCTTGCCATTGAAGCG
DLX2 RT-PCR FW	CTTACTCCGCCAAGAGCAG
DLX2 RT-PCR RV	TCCCGTTCACTATCCGAATTTC
FOXG1 RT-PCR FW	ACCTACTCCCTCAACCCCT
FOXG1 RT-PCR RV	AAAAGTAACTGGTCTGGCCC
FOXG1 5'UTR bisulfite FW	TGGTTGTTGTTTTTGTTATATGATTT
FOXG1 5'UTR bisulfite RV	ACTTAAAAATCATTTTCACCTCTTTC
GABRA2 RT-PCR FW	CATTTGTGTTCTCTGCCCTAATTG
GABRA2 RT-PCR RV	CTGTATCATAACGGAAGCCTTTTC
GRHL2 RT-PCR FW	AAGTCCAGTTTCACCAGAGG
GRHL2 RT-PCR RV	CTTCGGGTATTGAATGGAGG
GRHL3 RT-PCR FW	GATATCCTGAAAACCTCCCCG
GRHL3 RT-PCR RV	ACTCGCCTGACTTGATGTG
MT-ND1 PCR FW	ACGCCATAAAACTCTTCACCAAAG
MT-ND1 PCR RV	GGGTTCATAGTAGAAGAGCGATGG
MT-ND4 PCR FW	ACCTTGGCTATCATCACCCGAT
MT-ND4 PCR RV	AGTGCGATGAGTAGGGGAAGG
OPA1 genotyping FW	GGCATCTCGAATCACCGTCTCTGACACC
OPA1 genotyping RV	GGTGCCTGTCAGGCTCTTGCGG
OPA1 gRNA1 top	CACCGCGACTACGTCGGGCCGCTG
OPA1 gRNA1 bottom	AAACCAGCGGCCCGACGTAGTCGC
OPA1 gRNA2 top	CACCGCTGGGCTTACGTTCGGAGC
OPA1 gRNA2 bottom	AAACGCTCCGAACGTAAGCCCAGC
OPA1 isoform 1 RT-PCR FW	AGACCTTGTAAAGTTAGCACCAG
OPA1 isoform 1 RT-PCR RV	TGTCTGACACCTTTCTAAAATGC
OPA1 total isoform RT-PCR FW	CCAGCAAGATTAGCTACGAGAC
OPA1 total isoform RT-PCR RV	CACAATGTCAGGCACAATCC
PAX6 RT-PCR FW	CTAAGGATGTTGAACGGGCA
PAX6 RT-PCR RV	TTCTCCGTTGGAACTGATGG
SIX6 RT-PCR FW	GACAAAGGGACCGAGCG
SIX6 RT-PCR RV	CTTGCTGGATAGACTGGCG
SLITRK2 RT-PCR FW	GGAGATGGGCAGGATTTAGT
SLITRK2 RT-PCR RV	ACACTGAGGAACCAAACGC
TAF9B RT-PCR FW	CGATTAAGTGTTGGTGCTGTTAG
TAF9B RT-PCR RV	GTGGACTGAGAAGGTGGAATC

TBR1 RT-PCR FW	AACAATGGGCAGATGGTGGTT
TBR1 RT-PCR RV	GTTCACTTCCACCACATGCA
THUMPD2 RT-PCR FW	GTCAGCGACTCACAGTTACTAG
THUMPD2 RT-PCR RV	CACTTTCTGAAGGCAATGGC
VAX1 RT-PCR FW	TCTATCGGCTGGAGATGGAG
VAX1 RT-PCR RV	CCTGGTCCTTCTTCTGCTTG
VSX2 RT-PCR FW	ACCAGACCAAGAAACGGAAG
VSX2 RT-PCR RV	TTGAATGCCTTCTCCAGCTC
ZNF280D RT-PCR FW	TGTATCCCAACTTCTGAGCAC
ZNF280D RT-PCR RV	TCAGCCATGTTAGGTCTTGC
18S RRNA RT-PCR FW	CTACCACATCCAAGGAAGGCA
18S RRNA RT-PCR RV	TTTTTCGTCACTACCTCCCCG

Table S5. Antibodies used in this study. Related to Figures 1-6, Figure S1, and Figures S3-7.

Antibody name (Clone)	**Company**	**Catalog #**
Mouse anti-beta Actin (C4)	Santa Cruz	SC-47778
Mouse anti-DLX2 (B-5)	Santa Cruz	SC-393879
Rabbit anti-DNMT3A	Cell Signaling Technologies	2160S
Rabbit anti-DNMT3B	Sigma	HPA001595
Rabbit anti-DNM1L (D6C7)	Cell Signaling Technologies	8570S
Rabbit anti-FOXG1	Active Motif	61211
Rabbit anti-GAD1 (1G10.2)	Millipore	MAB5406
Mouse anti-GAD2 (A-3)	Santa Cruz	SC-377145
Rabbit anti-NANOG (D73G4)	Cell Signaling Technologies	4903S
Mouse anti-OCT3/4 (C-10)	Santa Cruz	SC-5279
Mouse anti-OPA1 (18/OPA1)	BD Biosciences	612606
Rabbit anti-PAX6 (D3A9V)	Cell Signaling Technologies	60433S
Sheep anti-PAX6	R&D Systems	AF8150
Rabbit anti-PKC (C24E6)	Cell Signaling Technologies	9368S
Mouse anti-TBR1 (G-5)	Santa Cruz	SC-376258
Mouse anti-ZO1 (ZO1-1A12)	Thermo Fisher Scientific	33-9100
Alexa-488 Donkey anti-mouse IgG	Thermo Fisher Scientific	A21202
Alexa-488 Donkey anti-sheep IgG	Thermo Fisher Scientific	A11015
Alexa-488 Goat anti-rabbit IgG	Thermo Fisher Scientific	A11034
Alexa-488 Rabbit anti-Ki67	Cell Signaling Technologies	11882S
Alexa-546 Donkey anti-mouse IgG	Thermo Fisher Scientific	A10036
Alexa-546 Donkey anti-rabbit IgG	Thermo Fisher Scientific	A10040
HRP Goat anti-mouse IgG	Jackson Immunoresearch	115-035-146
HRP Goat anti-rabbit IgG	Jackson Immunoresearch	111-035-144

Human ESC culture
The female hESC line WA#22 was obtained from the WiCell Research Institute (Madison, WI, USA) and maintained on mitomycin inactivated mouse embryonic fibroblast (MEF) layers. HESC media contained DMEM/F12, 15% human ESC-qualified fetal bovine serum (Biological Industries), 5% KnockOut Serum replacement, 1x non-essential aminoacids, 1x Glutamax, 50 µM Beta-mercaptoethanol (all from Thermo Fisher Scientific) supplemented with 5 ng/mL basic FGF (Miltenyi). 1 mg/mL Collagenase (Thermo Fisher Scientific) was used to passage hESCs.

Mouse experiments
MEFs and brain samples were isolated from embryonic day 13.5 old mouse embryos. Animal experiments were performed in accordance with protocols approved by the Animal Care Committee of the University of Oslo.

Generation of genetically modified WA#22 hESCs
Targeted knock-out of the *OPA1* gene was achieved using CRISPR-Cas9 technology. Human codon optimized SpCas9-expressing px330-U6-Chimeric_BB-CBh-hSpCas9 plasmid was a gift from Feng Zhang (Addgene plasmid # 42230). Oligonucleotides were designed using the http://crispr.mit.edu/ webtool, and annealed oligos were cloned into px330 plasmid according to the published protocol (Cong et al., 2013). Guide RNAs (sg1: 5'-GCGACTACGTCGGGCCGCTG-3'; sg2: 5´-GCTGGGCTTACGTTCGGAGC-3´) were used to target the human *OPA1* locus. hESCs were cultured in Rho Kinase (ROCK)-inhibitor (Y-27632; ATCC) 24 hours prior to electroporation. Cells were harvested using 0.25 % trypsin/ EDTA solution (Thermo Fisher Scientific) and 1 x 10_7 cells resuspended in 500 µl Opti-MEM (Thermo Fisher Scientific) were electroporated with 15 µg of each CRISPR plasmid (200 V, 500 µF, 0.4 cm cuvettes). Cells were subsequently plated on MEF feeder layers in hESC medium supplemented with ROCK-inhibitor for 48 hours. One week after electroporation, individual colonies were picked and expanded. *OPA1* deficient hESC clones were verified by PCR analysis and sequencing as described below. Two independent lines that slightly differed in their cut and repair mutation (*OPA1*+/- hESC #42 and #63) were derived. The majority of experiments were performed using clone #42. Key results were confirmed using clone #63 as indicated.

Genotyping
WA#22 cells were washed in PBS and lysed in 500 µl DNA lysis buffer (100 mM Tris pH 8.0, 5 mM EDTA, 0.2% SDS, 200 mM NaCl, 200 µg / ml proteinase K) overnight at 55 °C. DNA was precipitated using 100% isopropanol and washed with 70% ethanol. Genomic DNA was resuspended in 10 mM Tris pH 8.0, 0.1 mM EDTA and incubated at 55 °C overnight before subjected to PCR analysis. To verify deletion of *OPA1* exon 1, forward (FW) primer (5'-GGC ATC TCG AAT CAC CGT CTC TGA CAC C-3') and reverse (RV) primer (5'-GGT GCC TGT CAG GCT CTT GCG G-3') were used (wt: 750 bp; targeted allele: 450 bp).

Reprogramming of patient blood samples
Mononuclear cells were isolated from 20 mL of peripheral blood using Ficoll-Hypaque density gradient centrifugation as described (Ferrante and Thong, 1980). Blood was isolated from two male patients heterozygous for the OPA1 c.2873_2876delTTAG deletion (transcript ID: ENST00000361510.7), which causes a V958G/R959D substitution followed by a premature stop codon. 1x 10_6 MNC were cultured in alpha-MEM-10% FBS containing 20 ng/mL of each, thrombopoietin, stem cell factor, Flt3 ligand and interleukin-6 for 2 days before being transduced using OKSM Sendai virus (CytoTune™-iPS 2.0 (Thermo Fisher Scientific)) and spin infection (1650 rpm, 45 min). After centrifugation, cells were added to mitomycin-C inactivated MEFs, and hESC media was changed every 2 days. Up to five individual iPSC colonies were picked and

expanded from each of the two donors. The presence of the OPA1 c.2873_2876delTTAG deletion was confirmed by sequencing. Samples were obtained following informed consent using protocols conformed to the principles set out in the WMA Declaration of Helsinki, and approved by the Regional Medical and Health Research Ethics Committee of South-East Norway.

Copy number analysis

High resolution sequencing was performed to detect genome wide copy number alterations (CNAs) in DNA samples isolated from hESCs. Quality control of the raw sequence data was performed using FastQC v0.11.3. The reads were aligned with Bowtie v2.2.6 against the human reference genome hg19 using the --sensitive preset option (Nasca et al., 2017). Concordantly aligned read pairs and reads with the mapping quality of at least 30 were extracted using SAMtools v1.5 (Li et al., 2009). Copy number alterations (CNAs) were detected using QDNAseq v.1.10.0 with a window size of 100 kbp (Scheinin et al., 2014), excluding the sex chromosomes X and Y. No high confidence CNAs were detected in *OPA1*+/+ and *OPA1*+/- hESCs (data not shown).

Neural differentiation

Neural differentiation was performed using dual-SMAD inhibition as described previously (Chambers et al., 2009, Shi et al., 2012). Briefly, single cell suspensions of hESCs were prepared using Accutase (Thermo Fisher Scientific) and $1x10^6$ cells were seeded into Matrigel (Corning) coated 12-well tissue-culture plates (Falcon) in MEF-conditioned hESC media supplemented with 20 ng/mL basic FGF and 10 µM Rock inhibitor. Next day media was changed to neural induction media supplemented with 10 µM SB431542 and 1 µM Dorsomorphin (both from Sigma). Rock inhibitor was withdrawn at day 2. At day 11, neuroepithelial layers were either harvested for analysis or dissociated into small clusters with cell scraper/P1000 tips, and passaged into poly-L-Lysine (PLL)/Laminin (both from Sigma) coated plates. NPCs were cultured in neural induction media supplemented with SB431542/Dorsomorphin until observance of neural rosettes with everyday media change. At day 15-16, when rosette structures started to appear, 20 ng/mL basic FGF was also added to neural induction media for 3 days to promote NPC survival and proliferation. At day 21, NPCs were harvested for downstream analysis or used for neuronal differentiation. For the latter, day 21 NPCs were harvested using Accutase (Life technologies) and seeded at 20,000 cells / cm^2 density on PLL / Laminin coated 6 well plates (Corning). Following a total of 3-6 weeks, N2/B27 neural differentiation media was changed every 2-4 days and successful terminal neuronal differentiation was determined by morphological changes under bright-field microscope or immunostainings with neuronal markers.

Rescue experiments were performed using the DNA methyltransferase inhibitor RG108 (Sigma). Before neural differentiation, hESCs were incubated for 7 days with different concentration of RG108 in hESC media, and the RG108 was also added during neural differentiation. Media was changed every day.

Protein extraction and immunoblotting

Total cell lysates were prepared with cell lysis buffer (10 mM Tris pH 7.5, 150 mM NaCl, 1 mM EDTA, 1% SDS, 0.5% Na-deoxycholate) supplemented with protease inhibitor (Thermo Fisher Scientific) and samples were sonicated at 4°C to shear DNA. Protein concentration was measured using BCA (Thermo Fisher Scientific) and equal amounts of proteins were loaded on 4-20% gradient gels (Bio-Rad) in SDS running buffer (25 mM Tris-base, 192 mM glycine, 0.1% SDS). Proteins were transferred into Immobilon-P PVDF membranes in transfer buffer (25 mM Tris-base, 192 mM glycine, 10% methanol). Membranes were blocked with 5% milk / 0.1% Tween-20 in TBS buffer (25 mM Tris-base, 137 mM NaCl, 2.7 mM KCl, pH was adjusted to 7.4) and incubated overnight with primary antibodies (1 µg/mL) at 4°C. Respective HRP-linked secondary antibodies (Jackson Immunoresearch) were used at 1 µg/mL concentration in blocking buffer for

4 hours at room temperature. Chemiluminescent imaging was performed using Bio-Rad Imaging system. Quantification of western blots was done using Bio-Rad software. Primary and secondary antibodies are listed in Table S5.

Analysis of mitochondrial morphology and DNA content

To analyze cellular mitochondrial distribution, hESCs were dissociated as single cells using Accutase (Thermo Fisher Scientific) and seeded on Matrigel coated plates in MEF-conditioned hESC media supplemented with 20 ng/mL basic FGF and 10 µM ROCK-inhibitor. Next day, cells were incubated overnight with 2 µL of Celllight mitochondria-GFP, BacMam 2.0 (mito-GFP) reagent per 10.000 cells according to the manufacturer's instructions. After 18 hours, cells were fixed with 2% methanol-free formaldehyde (Thermo Fisher Scientific) for 15 min. After washing twice with PBS, coverslips were mounted with ProLong Diamond antifade mountant (Thermo Fisher Scientific). Photographs were taken using a Zeiss LSM 800 confocal laser scanning microscope. Images were processed using Zeiss Zen software Blue edition.

To measure mitochondrial DNA content of cells, DNA was extracted using DNeasy Blood & Tissue kit (Qiagen) according to the manufacturer's instructions. DNA concentration was measured using Nanodrop instrument. Real-time PCR was performed as duplicates using 10 ng DNA for each reaction. Mitochondrial genes NADH-ubiquinone oxidoreductase chain 1 (*MT-ND1*) and *MT-ND4* genes were quantified and normalized to nuclear gene beta-2-microglobulin (*B2M*) to measure mitochondrial:nuclear DNA copy number ratio.

Mitochondrial Respiration and ROS Measurements

Oxygen consumption rate (OCR) was determined using the Seahorse XF Cell Mito Stress Test and Seahorse XFe96 Analyzer (Agilent). In brief, hESCs were seeded onto a Matrigel-coated XF96 cell culture microplate (Agilent) at a density of 20,000 cells per well and incubated at 37 ℃ overnight in hESC medium supplemented with 10 µM ROCK inhibitor. One hour before the analysis, culture medium was changed to Seahorse XF DMEM Medium, pH 7.4 (Agilent) supplemented with 2 mM glutamine, 1 mM pyruvate and 10 mM glucose.

Week 3 NPCs were harvested using Accutase and seeded onto a Matrigel-coated XF96 cell culture microplate at a density of 20,000 cells per well. Cells were cultured overnight in N2/B27 media before OCR measurements were performed as described above. To assess mitochondrial respiration in neurons, NPCs were initially seeded at 20,000 cells / cm_2 density in 6 well plates and differentiated into immature neurons for 7 - 10 days in N2/B27 media. Immature neurons were harvested using Accutase and seeded onto a Matrigel-coated XF96 cell culture microplate at a density of 10,000 cells per 96 well. Neurons were further differentiated for 2 weeks in N2 /B27 media in XF96 cell culture microplates before measuring oxygen consumption rates.

Selective inhibitors of mitochondrial electron transport chain: Oligomycin (1 µM), carbonyl cyanide p-(trifluoromethoxy) phenylhydrazone (FCCP) (2 µM), and rotenone/antimycin A (0.5 µM) were injected sequentially during the measurements at indicated times to assess different parameters of mitochondrial functions. Basal respiration was determined as OCR before injection of oligomycin minus OCR after injection of rotenone/antimycin A. ATP-linked respiration (here noted as ATP production) was determined as OCR before oligomycin injection minus OCR after oligomycin treatment. Maximal respiration was determined as the OCR after FCCP minus non-mitochondrial OCR (OCR after rotenone/antimycin A treatment). Values were normalized to protein concentrations, which were determined using the BCA protein assay kit (Thermo Fisher Scientific).

ROS levels were measured using the general oxidative stress indicator 5-(and 6-) chloromethyl-2',7'-dichlorodihydrofluorescein diacetate, acetyl ester (CM-H2DCFDA) (Thermo Fisher Scientific)

according to the manufacturer's instructions. Single cell suspensions were loaded with 2 µM CM-H2DCFDA for 20 min in a tissue culture incubator. After washing with PBS, cells were analyzed immediately using the BD FACSCanto flow cytometer and Kaluza software (Beckman Coulter). Arithmetic mean values of fluorescence intensity were used to quantify ROS levels.

Flow cytometry analysis of cell cycle and proliferation

Cell cycle analysis and proliferation were assessed using fluorescent DNA intercalating agent propidium iodide (PI) and Alexa Flour 488 - conjugated Ki-67 antibody. Single cell suspensions were fixed overnight at -80 °C with 90% ethanol / dH20. Cells were permeabilized with 0.25% Triton / PBS for 15 minutes and incubated with blocking solution 0.5% BSA / 0.1% Tween / PBS. Cells were incubated with Ki-67 antibody for 1 hour in dark at room temperature followed by incubation with 100 µg/mL RNase A for 15 min at 37 °C to block non-specific PI binding. Subsequently, DNA was labeled with 100 µg/mL PI for 15 min in dark at room temperature. After washing with PBS, cells were analyzed immediately using the BD FACSCanto flow cytometer. Kaluza Analysis Software (Beckman Coulter) was used for analysis and illustration of flow cytometer data.

Flow cytometry analysis of apoptosis

Analysis of early and late apoptosis was carried out using FITC Annexin V Apoptosis Detection Kit (BD Pharmingen) according to the manufacturer's instructions. Single cell suspensions in binding buffer were loaded with 5 µl Annexin V and 5 µl PI solutions for 15 min in dark at room temperature. To address sensitivity to apoptotic stimuli, cells were incubated with 50 mM hydrogen peroxide solution for 30 min (neurons) or 45 min (NPCs). Cells were washed with binding buffer before dye loading is performed. After washing with binding buffer, cells were analyzed immediately using the BD FACSCanto flow cytometer. Kaluza Analysis Software (Beckman Coulter) was used for analysis and illustration of flow cytometer data.

Live cell automated imaging

To measure the cell proliferation rate, hESCs were dissociated to single cells using Accutase (Thermo Fisher Scientific). After, an equal number of cells was seeded into Matrigel (Corning) coated 24-well tissue-culture plates (Falcon) in MEF-conditioned hESC media supplemented with 20 ng/mL basic FGF and 10 µM Rock inhibitor. Next day, the plate was placed in a tissue culture incubator equipped with an IncuCyte Live Cell Analysis System. The proliferation rate was analyzed using the IncuCyte Zoom software.

Immunostaining

Cells were fixed with 2% methanol-free formaldehyde (Thermo Fisher Scientific) for 15 min and permeabilized with 0.3% Triton/PBS for 10 min at room temperature. Cells were blocked in 1% BSA/ 2% FBS/ 0.1% Tween/ PBS solution for 30 minutes at room temperature and incubated with primary antibodies (5-8 µg/mL in PBS) overnight at 4°C or for 3 hours at room temperature. After PBS washings, samples were incubated with the respective Alexa-488 or Alexa-546 conjugated secondary antibodies (Thermo Fisher Scientific) used at 5 µg/mL concentration for 3 hours at room temperature and nuclei were stained with DAPI. Samples were mounted with ProLong Diamond antifade mountant (Thermo Fisher Scientific). Photographs were taken with Zeiss Axio Vert.A1 microscope equipped with an AxioCam MRm camera or Zeiss LSM 800 confocal laser scanning microscope. Images were processed using Zeiss Zen software Blue edition. Primary and secondary antibodies are listed in Table S5.

RNA isolation and qRT-PCR

Cells were lysed with Trizol reagent (Qiagen) and RNA was extracted with chloroform. Extracted RNA was further cleaned using the RNAeasy kit (Qiagen) and on-column DNA digestion according to the manufacturer's instructions. The ABI cDNA synthesis kit was used to transcribe 1 µg of RNA into cDNA. Real-time PCR reactions were prepared with 10 ng of cDNA, 1x SYBR green, and 1 µM of each primer. Samples were run as technical replicates in an ABI9600 Instrument or BioRAD instrument. Specificity of amplification was shown using Melt-Curve, and samples were analyzed using 2.5 % agarose gels. The expression value was calculated based on the Delta-Delta-CT method and normalized to expression of the housekeeping gene 18S rRNA. Primer sequences are listed in Table S4.

Statistical analysis

Visualization and statistical analysis of data was performed using GraphPad Prism. Data is presented as mean ± standard error of mean (SEM). Student's t-test was used to analyze the differences between groups. * = $p < 0.05$, ** = $p < 0.01$, *** = $p < 0.001$

Patch clamp experiments

One coverslip with hESC-derived neurons was taken out of the incubator and transferred to a recording chamber where the cells were submerged in artificial cerebrospinal fluid (aCSF) (4.5 ml/min, 32 ± 1°C). The aCSF contained (in mM): 124 NaCl, 2 KCl, 1.25 KH_2PO_4, 2 $MgSO_4$, 2 $CaCl_2$, 26 $NaHCO_3$, 12 glucose (all from Sigma-Aldrich) and bubbled with a mixture of 95 % O_2 and 5 % CO_2. Visual guided patch clamping was performed with an Olympus microscope (BX51WI) with DIC optics and fitted with recording chamber and manipulators from Luigs and Neumann. Recording electrodes (Borosilicate 6-9 Mohm, O.D. 1.5 mm I.D. 0.86 mm with filament, Sutter Instrument) were filled with intracellular solution (120 mM potassium gluconate, 20 mM KCl, 10 mM EGTA, 2 mM $MgCl_2$, 2 mM Na_2ATP, 10 mM HEPES, pH adjusted to 7.3 with KOH). Axon Multiclamp 700B amplifier, Digidata 1440 and pClamp10 software (Molecular Devices) were used for recording and digitalizing the electrophysiological signals.

Transmission electron microscopy

hESC pellets were fixed in 2.5% glutaraldehyde in 0.1 M phosphate buffer overnight, and the pellets were subsequently post-fixed with 2% osmium tetroxide in 0.2 M cacodylate buffer. The cells were dehydrated with increasing concentration of ethanol, stained *en bloc* with 2% uranyl acetate in absolute ethanol. The final dehydration was carried out by two shifts of acetone. Then the pellets were infiltrated with mixtures of acetone and epoxy resin (Agar 100, Agar Scientific ltd): 33% epoxy, 50% epoxy, 67% epoxy and finally pure epoxy resin. The cell pellets were embedded in their Eppendorf tubes and polymerized overnight at 60°C.

Ultrathin sections of 70 nm were cut with an ultramicrotome (EMUC6, Leica), and mounted onto formvar-coated 0.75 x 2 mm slot grids, and subsequently stained with 4% uranyl acetate in 40% ethanol and Reynolds lead citrate. The sections were examined in an electron microscope (Tecnai Spirit Biotwin). For each cell population mitochondria from 10 cells were digitally photographed at a magnification of 11000. The average length of the mitochondria was measured using analySIS® (Olympus) software.

Samples for measurements of mitochondrial circumference and intercristae distance were fixed in 2% glutaraldehyde in 0.1 M PHEM buffer, followed by post-fixation in 2% OsO_4 and 1% potassium ferricyanide, and en bloc staining with 0.5% tannic acid and 1% Uranyl acetat. Dehydration was performed in ascending ethanol series followed by embedding in Epon. Ultrathin sections (80—100 nm) were cut on a Leica Ultracut and collected onto formvar-coated 100 mesh hexagonal grids. Images were acquired in a JEOL-JEM 1230 at 80 kV and recorded with a Morada camera (Olympus, Germany). For measuring mean circumference of mitochondria, images were taken at 15 kx in a systematic, uniform random fashion. Line intersections with the mitochondrial membrane were counted using a test lattice of 300 nm sidelength. 65 and 57 mitochondria were

counted from *OPA1+/+* and *OPA1+/-* hESCs, respectively. N = 2 experiments. Interchristae distances were determined counting N = 52 distances in *OPA1+/+* and N=105 distances in *OPA1+/-* conditions.

RNA sequencing

Integrity of the RNA samples was determined with Bioanalyzer (Agilent) and samples with an RNA Integrity number > 9 were used for sequencing. Libraries were prepared using Strand-specific TruSeq RNA-seq Sample Preparation Kit v2 (Illumina). Paired-end sequencing with 150 bp read-length was performed with a HiSeq 3000 machine.

Raw reads were aligned to the human genome (hg19), and splice junctions were mapped using TopHat v2.1.0 (Trapnell et al., 2012) with default parameters. Gene based read counts were obtained using featureCount v1.5.0-p1 (Liao et al., 2014) using default parameters. To perform normalization and statistical evaluation with negative binomial model between conditions on the count data, we used DESeq2 v1.10.1 Biconductor package (Love et al., 2014). Genes were considered differentially expressed when showing an absolute $\log_2$ fold change (treatment/control) ≥ 1.5 with adjusted p-value (padj) ≤ 0.05.

Bisulfite sequencing

DNA was prepared using DNeasy Blood & Tissue kit (Qiagen) and bisulfite conversion was performed with MethylEdge Bisulfite Conversion System (Promega) according to the manufacturer's protocol. Primers for PCR amplification of CpG island in *FOXG1* 5'UTR and *ATP10D* promoter were designed using MethPrimer program (Li and Dahiya, 2002). Primer sequences are listed in Table S4. PCR amplification of the target region in bisulfite converted DNA was achieved using EpiMark Hot Start Taq DNA polymerase (New England Biolabs) with 15-20 ng template DNA and confirmed by agarose gel electrophoresis.

Fresh PCR product (4 µL) was cloned into pCR4-TOPO (Thermo Fisher Scientific) vector according to the manufacturer's protocol. Briefly, 4 µL PCR product + 1 µL salt solution + 1 µL TOPO vector were mixed and incubated for 15 min at room temperature. Blue-white selection of transformed DH5alpha competent cells was done on IPTG/X-Gal (1 mM / 20 µg/mL) coated ampicillin selection (30 µg/mL) agar plates. White colonies were expanded in liquid LB media with 30 µg/mL ampicillin. Plasmids were prepared using Genejet Plamid Miniprep kit and sequenced using M13rev (-29) primer.

Quantification of DNA modifications and cellular metabolites using LC-MS/MS

DNA was added internal standard d_3-5-hydroxymethyl-2'-deoxycytidine (Toronto Research Chemicals) and hydrolyzed to deoxynucleosides by 20 U benzonase (Santa Cruz Biotech), 0.2 U nuclease P1, and 0.1 U alkaline phosphatase (Sigma) in 10 mM ammonium acetate pH 6.0 and 1 mM magnesium chloride at 40 °C for 45 min, then added 3 volumes of acetonitrile and centrifuged (16,000 g, 30 min, 4 °C). The supernatants were dried and dissolved in 50 µl water for LC-MS/MS analysis of modified and unmodified deoxyribonucleosides. Chromatographic separation was performed using an Agilent 1290 Infinity II UHPLC system with a ZORBAX RRHD Eclipse Plus C18 150 x 2.1 mm ID (1.8 µm) column protected with a ZORBAX RRHD Eclipse Plus C18 5 x 2.1 mm ID (1.8 µm) guard column (Agilent). The mobile phase consisted of water and methanol (both added 0.1 % formic acid), for 5-hm(dC) initially run at 0.15 mL/min with 5% methanol for 0.5 min, followed by a 4-min gradient of 5-15 % methanol, a flow increase to 0.25 mL/min and a 3 min gradient of 15-90 % methanol, then 4 min re-equilibration with 5 % methanol. A portion of each sample was diluted for the analysis of 5-methyl(dC) and unmodified deoxynucleosides. 5-methyl(dC) was chromatographed at 0.25 ml/min with a 3-min gradient of 5-90 % methanol, followed by 4 min re-equilibration with 5 % methanol, and unmodified deoxynucleosides were chromatographed isocratically with 20 % methanol. Mass spectrometric detection was performed using an Agilent 6495 Triple Quadrupole system operating in positive

electrospray ionization mode, monitoring the mass transitions 261.1/145.1 (d_3-5-hm(dC)), 258.1/142.1 (5-hm(dC)), 242.1/126.1 (5-m(dC)), 252.1/136.1 (dA), 228.1/112.1 (dC), 268.1/152.1 (dG), and 243.1/127.1 (dT).

S-adenosylmethionine (SAM) and S-adenosylhomocysteine (SAH) were measured by LC-MS/MS according to the method of Klepacki *et al* (Klepacki et al., 2013) with modifications optimized for cell lysates. Briefly, 100 µL cell lysate made up in 0.1% formic acid (FA) was mixed with 100 µL internal standard mix (5 µM $^{2}H_3$-SAM and 5 µM $^{13}C_5$-SAH), also prepared in 0.1 % FA. Samples were vortexed for 5 minutes followed by incubation on ice for 10 minutes. Extracted samples were then centrifuged at 13,000 rpm for 10 min and 60 µL supernatant was transferred to HPLC vials and 4 µL were injected into the LC-MS/MS system. SAM and SAH were separated on a Nexera N2 (Shimadzu) equipped with a SunFire C8, 4.6 x 100 mm and 3.5 µm particle size column (Waters GmbH, Eschborn) under isocratic conditions and mass transitions were monitored with a QTrap 6500+ (Sciex, Darmstadt). A flow of 0.75 mL /minute of 5 % Methanol and 95 % Water (both containing 0.1 % FA) was used to analyze SAM and SAH. The protonated molecular ions $[M+H]^+$ were: SAM (m/z = 399.0), $^{2}H_3$-SAM (m/z = 402.0), SAH (m/z = 385.1) and $^{13}C_5$-SAH (m/z = 390.0). The product ions were: SAM (m/z = 250.1 and m/z = 136.2), $^{2}H_3$-SAM (m/z = 250.1 and m/z = 136.2), SAH (m/z = 136.2), and $^{13}C_5$-SAH (m/z = 137.2). Quantification was carried by a calibration curve prepared under the exact same conditions. The linear range of calibrators under our experimental conditions is 0-1200 nM for both metabolites. SAM and SAH concentrations were normalized by the total concentration of protein in the lysate. Total protein concentration was determined with the BCA assay (Thermo Fisher Scientific).

Alpha-ketoglutarate and succinate were quantified according to a published LC-MS/MS method (Mullen et al., 2014) with modifications in sample preparation as follows: Cells were harvested as described above and washed with PBS prior to storage at -80 ^{o}C as dry cell pellets. Dry cell pellets were resuspended with aqueous 0.1 % FA and subjected to three cycles of freeze-thawing by alternating dry-ice and water-bath incubation at 25 ^{o}C. Subsequent vortexing, concentration, metabolite reconstitution, sample running and analysis were performed as described in the literature (Mullen et al., 2014). A twelve-point calibration curve was utilized to quantify each metabolite with a linear range of 0 to 500 µM.

References

AKEPATI, V. R., MULLER, E. C., OTTO, A., STRAUSS, H. M., PORTWICH, M. & ALEXANDER, C. 2008. Characterization of OPA1 isoforms isolated from mouse tissues. *J Neurochem,* 106**,** 372-83.

CHAMBERS, S. M., FASANO, C. A., PAPAPETROU, E. P., TOMISHIMA, M., SADELAIN, M. & STUDER, L. 2009. Highly efficient neural conversion of human ES and iPS cells by dual inhibition of SMAD signaling. *Nat Biotechnol,* 27**,** 275-80.

CONG, L., RAN, F. A., COX, D., LIN, S., BARRETTO, R., HABIB, N., HSU, P. D., WU, X., JIANG, W., MARRAFFINI, L. A. & ZHANG, F. 2013. Multiplex Genome Engineering Using CRISPR/Cas Systems. *Science,* 339**,** 819-823.

DELETTRE, C., GRIFFOIN, J. M., KAPLAN, J., DOLLFUS, H., LORENZ, B., FAIVRE, L., LENAERS, G., BELENGUER, P. & HAMEL, C. P. 2001. Mutation spectrum and splicing variants in the OPA1 gene. *Hum Genet,* 109**,** 584-91.

DELETTRE, C., LENAERS, G., GRIFFOIN, J. M., GIGAREL, N., LORENZO, C., BELENGUER, P., PELLOQUIN, L., GROSGEORGE, J., TURC-CAREL, C., PERRET, E., ASTARIE-DEQUEKER, C., LASQUELLEC, L., ARNAUD, B., DUCOMMUN, B., KAPLAN, J. & HAMEL, C. P. 2000. Nuclear gene OPA1, encoding a mitochondrial dynamin-related protein, is mutated in dominant optic atrophy. *Nat Genet,* 26**,** 207-10.

FERRANTE, A. & THONG, Y. H. 1980. Optimal conditions for simultaneous purification of mononuclear and polymorphonuclear leucocytes from human blood by the hypaque-ficoll method. *Journal of Immunological Methods,* 36**,** 109-117.

KLEPACKI, J., BRUNNER, N., SCHMITZ, V., KLAWITTER, J., CHRISTIANS, U. & KLAWITTER, J. 2013. Development and validation of an LC-MS/MS assay for the quantification of the trans-methylation pathway intermediates S-adenosylmethionine and S-adenosylhomocysteine in human plasma. *Clinica Chimica Acta,* 421**,** 91-97.

LI, H., HANDSAKER, B., WYSOKER, A., FENNELL, T., RUAN, J., HOMER, N., MARTH, G., ABECASIS, G., DURBIN, R. & GENOME PROJECT DATA PROCESSING, S. 2009. The Sequence Alignment/Map format and SAMtools. *Bioinformatics,* 25**,** 2078-2079.

LI, L.-C. & DAHIYA, R. 2002. *Methprimer: Designing Primers for Methylation PCRs*.

LIAO, Y., SMYTH, G. K. & SHI, W. 2014. featureCounts: an efficient general purpose program for assigning sequence reads to genomic features. *Bioinformatics,* 30**,** 923-30.

LOVE, M. I., HUBER, W. & ANDERS, S. 2014. Moderated estimation of fold change and dispersion for RNA-seq data with DESeq2. *Genome Biol,* 15**,** 550.

MULLEN, ANDREW R., HU, Z., SHI, X., JIANG, L., BOROUGHS, LINDSEY K., KOVACS, Z., BORIACK, R., RAKHEJA, D., SULLIVAN, LUCAS B., LINEHAN, W. M., CHANDEL, NAVDEEP S. & DEBERARDINIS, RALPH J. 2014. Oxidation of Alpha-Ketoglutarate Is Required for Reductive Carboxylation in Cancer Cells with Mitochondrial Defects. *Cell Reports,* 7**,** 1679-1690.

NASCA, A., RIZZA, T., DOIMO, M., LEGATI, A., CIOLFI, A., DIODATO, D., CALDERAN, C., CARRARA, G., LAMANTEA, E., AIELLO, C., DI NOTTIA, M., NICETA, M., LAMPERTI, C., ARDISSONE, A., BIANCHI-MARZOLI, S., IAROSSI, G., BERTINI, E., MORONI, I., TARTAGLIA, M., SALVIATI, L., CARROZZO, R. & GHEZZI, D. 2017. Not only dominant, not only optic atrophy: expanding the clinical spectrum associated with OPA1 mutations. *Orphanet J Rare Dis,* 12**,** 89.

SCHEININ, I., SIE, D., BENGTSSON, H., VAN DE WIEL, M. A., OLSHEN, A. B., VAN THUIJL, H. F., VAN ESSEN, H. F., EIJK, P. P., RUSTENBURG, F., MEIJER, G. A., REIJNEVELD, J. C., WESSELING, P., PINKEL, D., ALBERTSON, D. G. & YLSTRA, B. 2014. DNA copy number analysis of fresh and formalin-fixed specimens by shallow whole-genome sequencing with identification and exclusion of problematic regions in the genome assembly. *Genome Research*.

SHI, Y., KIRWAN, P. & LIVESEY, F. J. 2012. Directed differentiation of human pluripotent stem cells to cerebral cortex neurons and neural networks. *Nat Protoc,* 7**,** 1836-46.

TRAPNELL, C., ROBERTS, A., GOFF, L., PERTEA, G., KIM, D., KELLEY, D. R., PIMENTEL, H., SALZBERG, S. L., RINN, J. L. & PACHTER, L. 2012. Differential gene and transcript expression analysis of RNA-seq experiments with TopHat and Cufflinks. *Nat Protoc,* 7**,** 562-78.